

Gravitational collapse in 2+1 dimensional AdS spacetime

Frans Pretorius^{1*} and Matthew W. Choptuik^{1,2,3 †}

¹ Department of Physics and Astronomy, University of British Columbia,
Vancouver BC, V6T 1Z1 Canada

² CIAR Gravity and Cosmology Program

³ Center for Relativity, University of Texas at Austin, TX 78712-1081 USA

October 22, 2018

Abstract

We present results of numerical simulations of the formation of black holes from the gravitational collapse of a massless, minimally-coupled scalar field in 2+1 dimensional, axially-symmetric, anti de-Sitter (AdS) spacetime. The geometry exterior to the event horizon approaches the BTZ solution, showing no evidence of scalar ‘hair’. To study the interior structure we implement a variant of black-hole excision, which we call singularity excision. We find that interior to the event horizon a strong, spacelike curvature singularity develops. We study the critical behavior at the threshold of black hole formation, and find a continuously self-similar solution and corresponding mass-scaling exponent of approximately 1.2. The critical solution is universal to within a phase that is related to the angle deficit of the spacetime.

1 Introduction

The past several years has seen growing interest in the properties and dynamics of asymptotically anti de-Sitter (AdS) spacetimes, predominantly due to the discovery of black hole solutions in 2+1 dimensional AdS spacetime [1] and the AdS/CFT conjecture [2]. The existence of vacuum ¹ black holes (also called BTZ black holes) is surprising because the local solution to the field equations is isometric to AdS, and hence has constant curvature. What makes a BTZ spacetime different from AdS is its global structure, which can be obtained by making appropriate identifications within the universal covering space of AdS [3]. The natural question that such a construction poses is: how similar are these black holes to their more familiar 3+1 dimensional (4D) counter-parts? In particular, do these black holes have thermodynamic properties when considered within the framework of a quantum theory, and can they form through dynamical collapse processes? It turns out that BTZ black holes *do* bear striking resemblance to 4D black holes in many respects (see [4] for review articles). In this paper we present the results of a numerical study of the collapse and formation of non-rotating BTZ black holes from a massless scalar field in 2+1D AdS spacetime. Of particular interest is whether critical phenomena [5] are present at the *threshold* of black hole formation—namely if by fine-tuning of initial data, we can make the system asymptote (at “intermediate times”) to a solution which is universal in the sense of not depending on details of the initial data. Furthermore, if the black hole transition is “Type II”, so that there is *no* smallest mass of black hole which can be formed, then we expect their to be a scaling relation for the black hole mass of the form $M = K(p - p^*)^{2\gamma}$. Here p is a parameter in a family of initial data such that $p = p^*$ is the critical solution, K is a family dependent constant and γ

*Electronic address: fransp@physics.ubc.ca

†Electronic address: choptuik@physics.ubc.ca

¹with a negative cosmological constant

is a universal exponent (see [6] for a recent review). The ‘extra’ factor of 2 in the exponent is expected for BTZ black holes—see section 3.2. As we will show, it turns out that the system *does* exhibit a continuously self-similar (CSS) solution in the critical limit, with a scaling exponent $\gamma = 1.2 \pm 0.05$.

Earlier works on black hole formation in AdS considered disks of dust [7], null radiation [8], thin dust rings [9], and the collision of point-particles [10]. In the case of dust-ring collapse Peleg and Steif found a scaling exponent of 1/2 at the transition between black hole and naked singularity formation. Birmingham and Sen found the same exponent at the threshold of formation in the case of colliding particles. Husain and Olivier have also studied the massless scalar field in 2+1 dimensions using a double null formalism, and have formed black holes with their code [11].

Our paper is organized as follows. In section 2 we describe the system of coordinates and numerical scheme we have chosen to use, and the resultant field equations and boundary conditions. An interesting consequence of our analysis is that we are unable to derive boundary conditions for the scalar field at the edge of the universe that are analogous to the out-going radiation conditions often employed in numerical relativity. In AdS spacetime the scalar field reaches time-like infinity \mathcal{I} in *finite* proper time as measured by a central observer, and the only consistent boundary conditions we can place on the scalar field confine it to the universe. This is reassuring from the standpoint of global energy conservation, but complicates the search for the universal scaling relation between black hole mass and parameter-space distance to the critical solution. The system behaves as if the scalar field is within a finite sized box, and so when a black hole forms all of the scalar field initially present eventually falls into the hole. $M(p)$ is therefore trivially a function of how the initial energy distribution scales with p .

In section 3 we present results from the evolution of several families of initial data, focusing on critical behavior. To obtain γ , we follow the work of Garfinkle and Duncan[12], and examine the scaling of the maximum value attained by the curvature scalar R in the sub-critical regime. We also study the effect that a central point particle (characterized by the angle deficit of the spacetime) has on the critical solution. As expected, we find that the more massive the point particle, the smaller the initial amplitude of the scalar field that gives rise to the critical solution. One might thus expect to have a one-parameter family of critical solutions with an overall scale related to the particle mass. It *is* surprising, therefore, that the scalar field always grows to the *same* amplitude in a near-critical evolution. A phase shift in central proper time is the only qualitative difference attributable to the mass of the particle. At the end of section 3 we study the interior structure of black holes that form, giving evidence that a ‘crushing’ spacelike curvature singularity forms within the event horizon. Thus the interior structure is significantly different from the BTZ solution, which has constant curvature (though the BTZ singularity is still crushing for extended objects falling into it).

2 The Einstein Klein-Gordon system in AdS spacetime

We solve the Einstein field equations in 3 spacetime dimensions with cosmological constant $\Lambda \equiv -1/\ell^2$, coupled to a massless Klein-Gordon (KG) field

$$R_{ab} - \frac{1}{2}Rg_{ab} + \Lambda g_{ab} = \kappa T_{ab}, \quad (1)$$

where the stress-energy-momentum tensor for the KG field ϕ is [13]

$$T_{ab} = \phi_{;a}\phi_{;b} - \frac{1}{2}g_{ab}\phi_{;c}\phi^{;c}. \quad (2)$$

Covariant differentiation is denoted by a semi-colon, while a comma denotes partial differentiation. We only consider circularly symmetric configurations of a minimally-coupled scalar field in this paper. Hence, ϕ satisfies the wave equation

$$\square\phi = \phi_{;a}{}^a = 0, \quad (3)$$

and in coordinates (t, r, θ) adapted to the symmetry, characterized by the Killing vector $\partial/\partial\theta$, $\phi(r, t)$ is only a function of the radial coordinate, r , and time coordinate, t .

One of the many peculiar features of AdS spacetime is its causal structure. In particular, null infinity \mathcal{I} is time-like, and any observer living in AdS spacetime can send and receive light-like signals to and from \mathcal{I} in finite proper time [14]. These properties of AdS make it challenging to deal with numerically, as the scalar field traverses the entire universe on a local dynamical time-scale. Also, as we will show in section 2.1, the only regular boundary conditions on the field ϕ at \mathcal{I} are Dirichlet conditions, so we cannot ignore the unusual causal structure of the spacetime by, for instance, placing out-going radiation boundary conditions on ϕ at a finite proper distance from the origin. For these reasons, we adopt a coordinate system in which the metric takes the form:

$$ds^2 = \frac{e^{2A(r,t)}}{\cos^2(r/\ell)} (dr^2 - dt^2) + \ell^2 \tan^2(r/\ell) e^{2B(r,t)} d\theta^2. \quad (4)$$

$A(r, t)$ and $B(r, t)$ are arbitrary functions of (r, t) , and it is straight-forward to show that when $A = B = 0$ the above metric describes AdS spacetime; i.e. it is a solution to (1) with $T_{ab} = 0$. Notice that, in this metric, radial null geodesics travel with constant coordinate speed $dr/dt = \pm 1$, and \mathcal{I} is at $r = \pi\ell/2$. The metric is singular at \mathcal{I} , but we can place regular boundary conditions on A and B there, so that the spacetime is asymptotically AdS. Also, if we interpret θ as a periodic angular variable then the above metric has the correct topology to represent a BTZ black hole, as the topological censorship theorems require that the boundary at infinity share the topology of any event horizon that may exist in the interior of the spacetime [15]. However, for the non-rotating collapse described in this paper, θ has no dynamical significance.

Defining

$$\Phi(r, t) = \phi_{,r}, \quad \Pi(r, t) = \phi_{,t} \quad (5)$$

and using units where $\kappa = 4\pi$, we get the following set of equations upon expanding (1)–(3) with the metric (4):

$$A_{,rr} - A_{,tt} + \frac{(1 - e^{2A})}{\ell^2 \cos^2(r/\ell)} + 2\pi(\Phi^2 - \Pi^2) = 0, \quad (6)$$

$$B_{,rr} - B_{,tt} + B_{,r} \left(B_{,r} + \frac{2}{\ell \cos(r/\ell) \sin(r/\ell)} \right) - (B_{,t})^2 + \frac{2(1 - e^{2A})}{\ell^2 \cos^2(r/\ell)} = 0, \quad (7)$$

$$B_{,rr} + B_{,r} \left(B_{,r} - A_{,r} + \frac{1 + \cos^2(r/\ell)}{\ell \cos(r/\ell) \sin(r/\ell)} \right) - \frac{A_{,r}}{\ell \cos(r/\ell) \sin(r/\ell)} - A_{,t} B_{,t} + \frac{(1 - e^{2A})}{\ell^2 \cos^2(r/\ell)} + 2\pi(\Phi^2 + \Pi^2) = 0, \quad (8)$$

$$B_{,rt} + B_{,t} \left(B_{,r} - A_{,r} + \frac{\cot(r/\ell)}{\ell} \right) - A_{,t} \left(B_{,r} + \frac{1}{\ell \sin(r/\ell) \cos(r/\ell)} \right) + 4\pi\Phi\Pi = 0 \quad (9)$$

and

$$[\tan(r/\ell) e^B \Phi]_{,r} - \tan(r/\ell) [e^B \Pi]_{,t} = 0. \quad (10)$$

Within the context of the 3+1, or ADM, formalism, equations (8) and (9) are the Hamiltonian and momentum constraints respectively, while equations (6) and (7) are combinations of the evolution and constraint equations. Equation (10) is the wave equation for the scalar field. There are two unknown geometric variables— $A(r, t)$ and $B(r, t)$; hence one needs to use at least two of the four equations (6) - (9) to dynamically determine the geometry. In this work, we have chosen to use equations (6) and (7) to update A and B . As is common practice in such a “free evolution scheme”, we can then use residuals of the constraints (8) and (9) as one way of estimating the level of error in our solution.

With regards to initial conditions, we choose to freely specify $\Phi(r, 0)$ and $\Pi(r, 0)$ (we *have* to specify two scalar-field degrees of freedom at each r), as well as $B(r, 0)$ and $B_{,t}(r, 0)$. $A(r, 0)$ and $A_{,t}(r, 0)$ are then fixed

from the constraint equations (see sec. 2.2 for more details). This procedure is clearly somewhat *ad hoc*, but has worked very well in our study.

The Ricci scalar of this spacetime is

$$R = \frac{4\pi \cos(r/\ell)^2}{e^{2A}\ell^2} (\Phi^2 - \Pi^2) - \frac{6}{\ell^2}. \quad (11)$$

The Weyl tensor is zero, and other non-zero curvature scalars can be expressed as polynomial functions of R .

2.1 Regularity conditions

We require that the solution for our dynamical variables $A(r, t)$, $B(r, t)$, $\Phi(r, t)$ and $\Pi(r, t)$ be regular at the origin, $r = 0$, and at \mathcal{I} , $r = \pi\ell/2$. The field equations then essentially dictate the allowed boundary conditions on these variables. By inspection of (6)–(10) we obtain the following conditions. At $r = 0$

$$A_{,t}(0, t) = B_{,t}(0, t) \quad (12)$$

$$A_{,r}(0, t) = 0 \quad (13)$$

$$B_{,r}(0, t) = 0 \quad (14)$$

$$\Phi(0, t) = 0 \quad (15)$$

$$\Pi_{,r}(0, t) = 0 \quad (16)$$

and at $r = \pi\ell/2$

$$A(\pi\ell/2, t) = A_{,r}(\pi\ell/2, t) = A_{,t}(\pi\ell/2, t) = 0 \quad (17)$$

$$B_{,r}(\pi\ell/2, t) = 0 \quad (18)$$

$$\Phi(\pi\ell/2, t) = 0 \quad (19)$$

$$\Pi(\pi\ell/2, t) = 0. \quad (20)$$

Note that condition (16) on $\Pi(0, t)$ is a direct consequence of the defining relation for $\Pi(r, t)$ (5), and the regularity condition for $\Phi(0, t)$ (15). Also note that we have multiple conditions for B at the outer boundary, and for A and B at the origin. We have chosen to implement the Neumann conditions for A and B at the origin and the Dirichlet condition for A at \mathcal{I} , and then to monitor the other conditions as a consistency check during evolution. Conditions (17)–(20) ensure that the spacetime is asymptotically AdS.

It is interesting that the field equations enforce Dirichlet boundary conditions on Φ and Π , effectively preventing us from implementing out-going radiation boundary conditions at \mathcal{I} (if we wanted to let the field “leak out of the universe” when it reaches \mathcal{I}). To see this more clearly, consider the energy fluxes $T_{ab}\eta^a\eta^b$ and $T_{ab}\ell^a\ell^b$ along outgoing and ingoing null vectors, ℓ^a and η^a , respectively, normalized so that $\ell^a\eta_a = -1$

$$\ell^a = \frac{\cos(r/\ell)}{\sqrt{2}e^A} \left[\frac{\partial}{\partial t} + \frac{\partial}{\partial r} \right]^a \quad (21)$$

$$\eta^a = \frac{\cos(r/\ell)}{\sqrt{2}e^A} \left[\frac{\partial}{\partial t} - \frac{\partial}{\partial r} \right]^a \quad (22)$$

A straight forward calculation using (2) gives

$$E_{\pm} = \frac{\cos(r/\ell)^2(\Phi \pm \Pi)^2}{2e^{2A}}, \quad (23)$$

where E_+ is the influx and E_- the outflux. Thus no- outflux/influx boundary conditions can be obtained in the usual way by differentiating $\Phi \pm \Pi$ with respect to r and t in turn, and utilizing the fact that, from (5), $\Phi_{,t} = \Pi_{,r}$:

$$\Phi_{,r} \pm \Phi_{,t} = 0 \quad (24)$$

$$\Pi_{,r} \pm \Pi_{,t} = 0. \quad (25)$$

$$(26)$$

Here, the plus sign corresponds to no-influx, and the minus sign to no-outflux. However, at the outer boundary, regularity forces $\Phi(\pi\ell/2, t) = \Pi(\pi\ell/2, t) = 0$, and hence $\Phi_{,t}(\pi\ell/2, t) = \Pi_{,t}(\pi\ell/2, t) = 0$, so there is no distinction between the no-influx and no-outflux condition. The only situation consistent with both conditions is that *no* flux crosses the outer boundary in either direction. Even when we try to derive no-outflux/influx conditions with the asymptotic behavior of ϕ factored out, namely letting $\phi = \cos^2(r/\ell)\hat{\phi}$ and placing boundary conditions on $\hat{\phi}$, we find that the wave equation on \mathcal{I} cannot distinguish between no-outflux and no-influx conditions. Also, in early experiments we were unable to obtain stable numerical evolution with the no-influx boundary conditions (24) and (25) applied at a finite proper circumference, corresponding to $r < \pi\ell/2$. The Dirichlet boundary condition at \mathcal{I} is also consistent with the behavior of a massive scalar field in an AdS background, where an infinite effective-potential barrier prevents any of the field from reaching \mathcal{I} , regardless of how small the mass is. Of course, all of this does not mean that an effective outgoing radiation condition can not be implemented for the massless field in asymptotically AdS spacetimes. In any case, in the context of the current study, we would be apt to view such a condition as a numerical convenience, rather than being of any intrinsic physical interest.

2.2 Initial conditions

For initial conditions at $t = 0$, we are free to specify the scalar field gradients $\Phi(r, 0)$ and $\Pi(r, 0)$, the metric function $B(r, 0)$ and its time derivative $B_{,t}(r, 0)$. We then numerically solve for $A(r, 0)$ and $A_{,t}(r, 0)$ using the hamiltonian and momentum constraints (8) and (9). The freedom that we have to specify $B(r, 0)$ amounts to a choice of what the proper circumference, $(\ell \tan(r/\ell)e^B)$, and its initial time derivative are, as a function of the radial coordinate r . That we do not have the freedom to choose B for all time is a consequence of the gauge condition that radial light-like signals travel with unit coordinate velocity. For simplicity we set $B(r, 0) = B_{,t}(r, 0) = 0$.

We believe (though are unable to prove so), that the set of conditions just described is capable of generating all possible initial data, which is regular and free of trapped surfaces, for the minimally-coupled scalar field in asymptotically AdS spacetime (in 2+1 dimensions). The presence of trapped surfaces at $t = 0$ is incompatible with the conditions on $B(r, 0)$ and $B_{,t}(r, 0)$ —in our coordinate system $dr/dt = 1$ along an outgoing null curve, and hence a non-zero $B(r, 0)$ and/or $B_{,t}(r, 0)$ is required to describe non-positive outward null-expansion. However, in this study we are only interested in initial data that *is* free of trapped surfaces, so the conditions on $B(r, 0)$ and $B_{,t}(r, 0)$ are not restrictive.

For the initial scalar field profile, $\phi(r, 0)$, we consider three families of functions—a gaussian curve raised to the n^{th} power

$$\phi(r, 0) = P e^{((r-r_0)/\sigma)^{2n}}, \quad (27)$$

a ‘kink’ (based on an arctan function) for which $\Phi = \partial\phi/\partial r$ is

$$\Phi(r, 0) = \frac{-2P\sqrt{\sigma} \cos(r/\ell) \sin(r/\ell) [-\ell \sin(r/\ell) \cos(r/\ell) + 2(r-r_0)(1-2\sin(r/\ell)^2)] e^{-(r-r_0)^2/\sigma^2}}{\pi\ell [\sigma \sin(r/\ell)^4 \cos(r/\ell)^4 + (r-r_0)^2]} \quad (28)$$

and a family of harmonic functions ²

$$\phi(r, 0) = P \cos^2(rn/\ell), \quad (29)$$

where P, r_0, σ and n are constant parameters. Then, depending upon whether we want to model initially ingoing, outgoing or static fields, we set $\Pi(r, 0) = \Phi(r, 0)$, $\Pi(r, 0) = -\Phi(r, 0)$ or $\Pi(r, 0) = 0$ respectively. Note that this method cannot give purely ingoing or outgoing pulses— $\Pi(r, t) = \pm\Phi(r, t)$ is *not* an exact solution to the wave equation, and a little bit of energy always propagates in the opposite direction to that desired.

As noted previously, we set $B(r, 0) = B_{,t}(r, 0) = 0$. The remaining geometric variables, $A(r, 0)$ and $A_{,t}(r, 0)$ are then computed from the Hamiltonian and momentum constraints (8) and (9). We integrate the constraints outwards from $r = 0$, setting $A_{,t}(0, 0) = 0$. For the most part we will consider the collapse of

²we call these functions ‘harmonic’ because without back-reaction and for initially static configurations ($\Pi(r, 0) = 0$) the exact solution to the wave equation is periodic in time.

a scalar field initially exterior to empty AdS space. This corresponds to setting $A(0,0) = 0$. However, in section 3.2.2, we will briefly consider the effect of collapsing the field in the presence of a point particle at the origin, the calculation of which involves introducing an angle deficit into the spacetime. From the metric (or by examining the parallel transport of a vector about $r = 0$ in an infinitesimal loop), the angle deficit ω at $t = 0$ is related to $A(0,0)$ as follows:

$$\omega = 2\pi(1 - e^{A(0,0)}). \quad (30)$$

Of more interest is the relationship between $A(0,0)$ and the mass of the point-particle, M_{pp} . The remainder of this section is devoted to finding this relationship, and in the process we will define a general mass aspect function $M(r,t)$ for the spacetime.

When the scalar field gradients identically vanish (which they do at \mathcal{I} , and, to an excellent approximation, at $r = 0$ for the initial data that we consider), the Hamiltonian constraint has the simple solution

$$e^{2A} = \frac{k}{k - \cos^2(r/\ell)}, \quad (31)$$

where k is a constant of integration. We can relate k to the BTZ mass parameter M of the spacetime by appealing to the usual form in which the BTZ solution is expressed:

$$ds^2 = -(-M + \bar{r}^2/\ell^2)d\bar{t}^2 + \frac{1}{-M + \bar{r}^2/\ell^2}d\bar{r}^2 + \bar{r}^2d\theta^2. \quad (32)$$

$M = -1$ is AdS spacetime, $M \geq 0$ are black hole solutions and $M < 0, M \neq -1$ are spacetimes with conical singularities, or point particles at the origin (the range of \bar{r} is from 0 to ∞). For general (non-vacuum) solutions let us define the mass aspect $M(\bar{r}, \bar{t})$ as follows

$$|\nabla\bar{r}|^2 \equiv -M(\bar{r}, \bar{t}) + \bar{r}^2/\ell^2. \quad (33)$$

Then, in our coordinate system (4), $M(r,t)$ takes the following form

$$M(r,t) = e^{2(B-A)} [e^{2A} \tan^2(r/\ell) + \ell^2 \sin^2(r/\ell)((B_t)^2 - (B_r)^2) - 2\ell \tan(r/\ell)B_r - \sec^2(r/\ell)]. \quad (34)$$

Using the field equations (6)-(9) it is straightforward to show that M is a conserved quantity in regions of the spacetime where Φ and Π are zero (in particular at \mathcal{I}). At $t = 0$, where $B = B_t = 0$, we can substitute (31) into (34) to find k :

$$k = \frac{1}{1 + M}. \quad (35)$$

When $M \geq 0$ our metric (4) with the chosen initial conditions is singular at the horizon of an empty BTZ spacetime, but the metric turns out to be well behaved at $t = 0$ for initial data that does not contain trapped surfaces³.

Finally, from (31) and (35) the contribution, M_{pp} , of the point particle to the mass of the spacetime is

$$M_{pp} = 1 - e^{-2A(0,0)} \quad (36)$$

2.3 Numerical Scheme

We solve the set of equations (6),(7) and (10) by converting them to a system of finite difference equations on a uniform coordinate grid using a two-time level Crank-Nicholson scheme. We also add Kreiss-Oliger style dissipation [16] to control high-frequency solution components; this is crucial for the stability of our method.

At first, we used standard 2nd order accurate 3-point finite difference stencils for the spatial derivatives at each time level—centered-difference operators at interior points, a forward-difference operator at the inner

³however, because of our choice of gauge, we know that the coordinate system must become singular within one light-crossing time (LCT) of the formation of a black hole. The event horizon is a null hypersurface travelling outward with unit coordinate velocity, thus the coordinate distance between the event horizon and \mathcal{I} will go to zero within a time $t = \pi\ell/2$.

boundary and a backward-difference operator at the outer boundary. However, we found that these operators excited a small instability in the metric variables in the vicinity of the outer boundary. The resultant ripples would propagate inwards and cause problems in situations where black hole formation was imminent. The primary source of these ripples was truncation error in the solution A exciting small oscillations in B . Specifically, A acts as a source term in the evolution equation for B (7), and B happens to be very sensitive to small errors in A near the outer boundary (essentially since the leading term of A , when considered as a power series in $\cos^2(r/\ell)$, cancels with the spatial derivatives of B in (7) initially, and so higher order, less accurately known terms of A are responsible for B 's “acceleration”). To reduce these problems we now use a 5-point, 4th order accurate spatial derivative operator at interior grid points, and 6-point 4th order backward and forward operators near boundaries that have the same truncation error as the interior operator. Also, we find that using the momentum constraint (9) to solve for A at the next to last grid point is necessary to obtain convergence of the solution as we go to finer spatial resolution (for some as yet unknown reason the evolution equation was exciting a growing mode on finer grids at that point). The program to perform the evolution was written in Fortran 77 and RNPL (Rapid Numerical Prototyping Language [17]); animations and pictures from several evolutions can be obtained from our website [18].

2.4 Detecting black holes and excising singularities

To detect black hole formation we search for trapped surfaces, defined to be surfaces where the expansion of outgoing null curves normal to the surface is negative. If cosmic censorship holds, then trapped surfaces are always found within the event horizon of a black hole, though at the end of the simulation we can trace null rays backwards from \mathcal{I} to confirm this. In our coordinate system the condition for a surface to be trapped is

$$1 + \ell \cos(r/\ell) \sin(r/\ell)(B_{,r} + B_{,t}) < 0. \quad (37)$$

We estimate the mass of the black hole by monitoring the proper circumference $2\pi\ell \tan(r_{\text{AH}}/\ell)e^{B(r_{\text{AH}},t)}$ of the apparent horizon (the outer-most trapped surface), and use the relationship between BTZ black hole mass and event horizon circumference ((32)—the horizon is at $\bar{r} = \sqrt{M}\ell$):

$$M \approx \tan^2(r_{\text{AH}}/\ell)e^{2B(r_{\text{AH}},t)}. \quad (38)$$

If all of the scalar field is absorbed by the black hole during evolution, then the estimated mass should eventually become equal to the initial, asymptotic mass of the spacetime as given by (34) in the limit $r \rightarrow \pi\ell/2$.

As we will show in section 3.3, shortly after an apparent horizon(AH) forms, we find what appears to be a spacelike curvature singularity forming within the AH. If we use a straightforward evolution scheme, the metric and scalar field variables quickly diverge, and any given simulation just as quickly breaks down. At the same time, we would like to probe the structure of the spacetime approaching the singularity, as well as to continue to following the evolution outside the AH as long as our coordinate system allows (approximately 1 light-crossing time). To accomplish this, we have implemented *singularity excision*, a technique fundamentally motivated by the black-hole-excision strategy first proposed by Unruh [19].

Our excision strategy is as follows. We monitor the magnitude of the metric variables, and when they grow beyond a certain threshold ⁴ at any point we excise that point plus a small buffer zone (of 4 to 6 grid points) on either side of it. (Note that the non-excised region of the grid will no longer be contiguous if the excised point is further away from the original grid boundaries than the size of the buffer zone). At the new grid boundaries exterior to the excised region, we continue to solve for the metric and field variables using the evolution equations, but replace all centered-difference operators with forward and backward-difference operators, as appropriate, so that the solution is not “numerically influenced” by the excised grid points. Physically, the solution that one would obtain within the causal future of the excised zone is meaningless, so we also remove this region of the grid during subsequent evolution. In our coordinate system this is easy to implement, as radial null curves travel at constant, unit coordinate velocity. Thus, if our grid-spacing is Δr , after an amount of time $\Delta t = \Delta r$ we expand the excised region by 1 grid point on either side. Also, we continue to monitor the metric variables on the remainder of the grid, and when they grow beyond the

⁴for a threshold we choose a number that is sufficiently large so we are fairly certain (from past experiments) that if any variable grows beyond the threshold then a crash is imminent

threshold at any other points we expand the excised region to include those points (and a buffer). Thus the excised piece of the grid is always contiguous. In principle, it would not be difficult to keep track of multiple excised zones, though we did not find it necessary to do so for the interior solution shown in sec. 3.3—a single zone is sufficient to obtain a good view of all of the interior up to the putative spacetime singularity.

We have tested the singularity excision scheme by excising a light cone from a solution that remains regular, and verifying that the excised solution *does* converge to the regular solution as Δr decreases.

In summary, we briefly clarify the difference between singularity and black hole excision. First, notice that we never use trapped surfaces to trigger the excision of a region of the grid. Thus, our code could, without modification, excise naked and coordinate singularities. The boundary of the excised region is always null or spacelike, so the scheme might not be able to distinguish between timelike and null curvature singularities. However, if a timelike singularity was encountered, it may still be possible to deduce its nature by examining the curvature invariants just exterior to the excised surface. For example, suppose during evolution a light-like region was excised, and curvature invariants started diverging as one approached the initial excised point, yet remained relatively “small” and finite just outside the future light-cone of the excised point, then one would have reasonable evidence for a timelike singularity. Second, with the singularity excision scheme, we excise only the region of the grid to the causal future of the singularity. In the case of a black hole spacetime, this results in a more complete view of the spacetime than what one would obtain with the standard black hole excision strategy (which would have in Fig. 19, for example, excised the region of the spacetime labeled “region of trapped surfaces”, and everything to the left of it).

3 Results

In this section we discuss results from the evolution of several sets of initial data, focusing on the threshold of black hole formation. For convenience we set $\ell = 2/\pi$ so that \mathcal{I} is at $r = 1$, though the results presented here are valid for any non-zero, finite ℓ , through an appropriate rescaling of the metric variables and scalar field gradients. Specifically, consider the following coordinate transformation

$$\tilde{r} = \frac{r}{\ell}, \quad \tilde{t} = \frac{t}{\ell}, \quad (39)$$

with \tilde{r} defined on the range $[0, \pi/2]$. Then it is easy to see that the ℓ dependence cancels from all equations (6)-(10) when expressed in terms of \tilde{r} and \tilde{t} . So, given a solution $A(\tilde{r}, \tilde{t})$, $B(\tilde{r}, \tilde{t})$, $\Phi(\tilde{r}, \tilde{t})$ and $\Pi(\tilde{r}, \tilde{t})$ to the rescaled field equations we can find a corresponding solution for any ℓ by inverting the transformation (39) (see also (5)):

$$\begin{aligned} A(\tilde{r}, \tilde{t}) &\rightarrow A(r/\ell, t/\ell) \\ B(\tilde{r}, \tilde{t}) &\rightarrow B(r/\ell, t/\ell) \\ \Phi(\tilde{r}, \tilde{t}) &\rightarrow \ell\Phi(r/\ell, t/\ell) \\ \Pi(\tilde{r}, \tilde{t}) &\rightarrow \ell\Pi(r/\ell, t/\ell), \end{aligned} \quad (40)$$

with r ranging from 0 to $\pi\ell/2$. Notice that the initial energy density, being proportional to $(\Phi^2 + \Pi^2)$, scales like ℓ^2 , so there is no straight-forward method to extrapolate a solution to the limit of zero cosmological constant, where $\ell \rightarrow \infty$.

We present results from 4 families of initial data: an ingoing gaussian ((27) with $n = 1$), an ingoing squared gaussian ((27) with $n = 2$), an ingoing kink (28), and a time-symmetric, $n = 1$, harmonic function (29). In each case we vary the amplitude P when tuning to the black hole threshold⁵, and for the first three families we have chosen $\sigma = 0.05$ and $r_0 = 0.2$. Except in section 3.2.2, where we briefly study collapse onto a point-particle, we have set $A(0, 0) = 0$ in all cases, corresponding to angle deficit-free spacetimes. The 3 ingoing families were simulated using a finest numerical grid of size 4096 points, with a Courant factor of 0.1; thus 40960 time steps are required per light-crossing time (for some of the critical solutions presented in the next section a grid size of 8192 points was used with a Courant factor of 0.2) For the time-symmetric \cos^2 function we do not need as many points to get good convergence results (because of the milder field

⁵though we did check (for the gaussian) that we get the same critical solution when tuning the width, keeping the amplitude fixed

gradients), so that the highest resolution required for that family was a 1024-point grid. In fact, we get acceptable results even after 50 light-crossing times with 1024 points for the \cos^2 data, whereas the more compact ingoing families start having noticeable errors (estimated from convergence tests) in near-critical evolution after 3-4 LCT's with 4096 points.

Fig. 1 shows the initial scalar field gradient, $\Phi(r, 0)$, of typical amplitude for each of the families. Fig. 2 shows the metric function $A(r, 0)$ for a gaussian (the other families have similar shapes for A), and for later reference we show how $A(r, t)$ and $B(r, t)$ have evolved at $t = 0.6$. In order to provide the reader with some feeling for the dynamics of a “typical” evolution, Fig. 3 shows a “space-time” plot of the evolution of a sample gaussian with $P = 0.1302$ that does not form a black hole within 4 LCT's (and it should not, as the asymptotic mass of the spacetime is -1.062×10^{-2}).

3.1 Parameter space survey, varying P

Figs. 4 and 5 show plots of the asymptotic mass, $M(P)$, of the spacetime, as a function of the amplitude P , about the region $M = 0$ of parameter space, for the gaussian and harmonic families. The second curve on each plot shows the initial mass estimate of a black hole (if one formed during the 2 LCTs of the gaussian evolution, or 50 LCTs of the harmonic evolution) at the time an apparent horizon is first detected. For these amplitudes, Figs. 6 and 7 show the time t and coordinate position r of apparent horizon formation. Qualitatively, the features of corresponding plots for the kink and squared gaussian (also evolved for 2 LCT's) are very similar to those for the gaussian, so for brevity we do not show them. To within the resolution of our simulation, the final black hole mass always approaches the asymptotic mass—in other words, we do *not* detect any remnant scalar field (black hole ‘hair’). See Fig. 8 for typical examples. Due to the “reflecting” boundary conditions at time-like \mathcal{I} , this is not too surprising, although one might have expected something like a low amplitude, long wave-length, periodic scalar remnant. The scalar field also tends to zero at late times along the event horizon, though in that region of the spacetime our results are not good enough to obtain useful decay exponents.

Fig. 7 for the harmonic family shows almost chaotic dependence of the time of AH formation as a function of amplitude, as $M(P)$ decreases towards $M = 0$. There is evidence that this behavior is also present for the other families of initial data, but we have not run those simulations at the necessary resolution to give *convincing* evidence. What appears to be happening is the following. First of all, it is more “difficult” for a distribution of the scalar field corresponding to $M \gtrsim 0$ to form a black hole—the distribution needs to be compact and centrally condensed. Thus, when we implode a relatively “space-filling” distribution with M small (and positive) a black hole will not form on the first bounce through the origin. However, because of the boundary conditions at infinity, the scalar field will reflect off \mathcal{I} , and, as the field has evolved through a strong field (non-linear) regime in the interior, the distribution of energy will be different on the subsequent implosion. Moreover, because of the strong gravitational field, the scalar field has a tendency to spend more time in the vicinity of the origin on average, preventing it from dispersing throughout the spacetime. So, one may expect that if the asymptotic mass M is positive, a region of phase space will eventually be traversed during evolution, where it is favorable for a black hole to form, no matter how near-zero is M . However, due to the chaotic nature of the curve in Fig. 7, we cannot extrapolate $t_0(M)$ to $t_0 = \infty$ in order to directly test this conjecture.

3.2 The critical regime

To search for critical behavior in the gravitational collapse of the four families of initial data introduced in the previous section, we vary the amplitude P in each case to find the threshold of black hole formation. Ideally, we would simply seek the amplitude P^* where a black hole forms for $P > P^*$, while for $P < P^*$ the scalar field bounces around forever without collapse. Unfortunately, such a search is not practical; as mentioned in the previous section we do not have the computational resources to follow compact initial data for numerous LCT's, and, even with the \cos^2 data, we do not see any trends that would allow us to conclude that if a black hole has not formed after, say, n LCT's, then it probably will not form at all. Thus, what we do instead is tune to the threshold of black hole formation on the initial implosion; i.e. we base our search on whether or not a black hole forms *before* any initially out-going radiation reflects off \mathcal{I} and then falls in, contributing to the collapse. This point of parameter space is labeled as P^* in Figs. 4 and 5, and

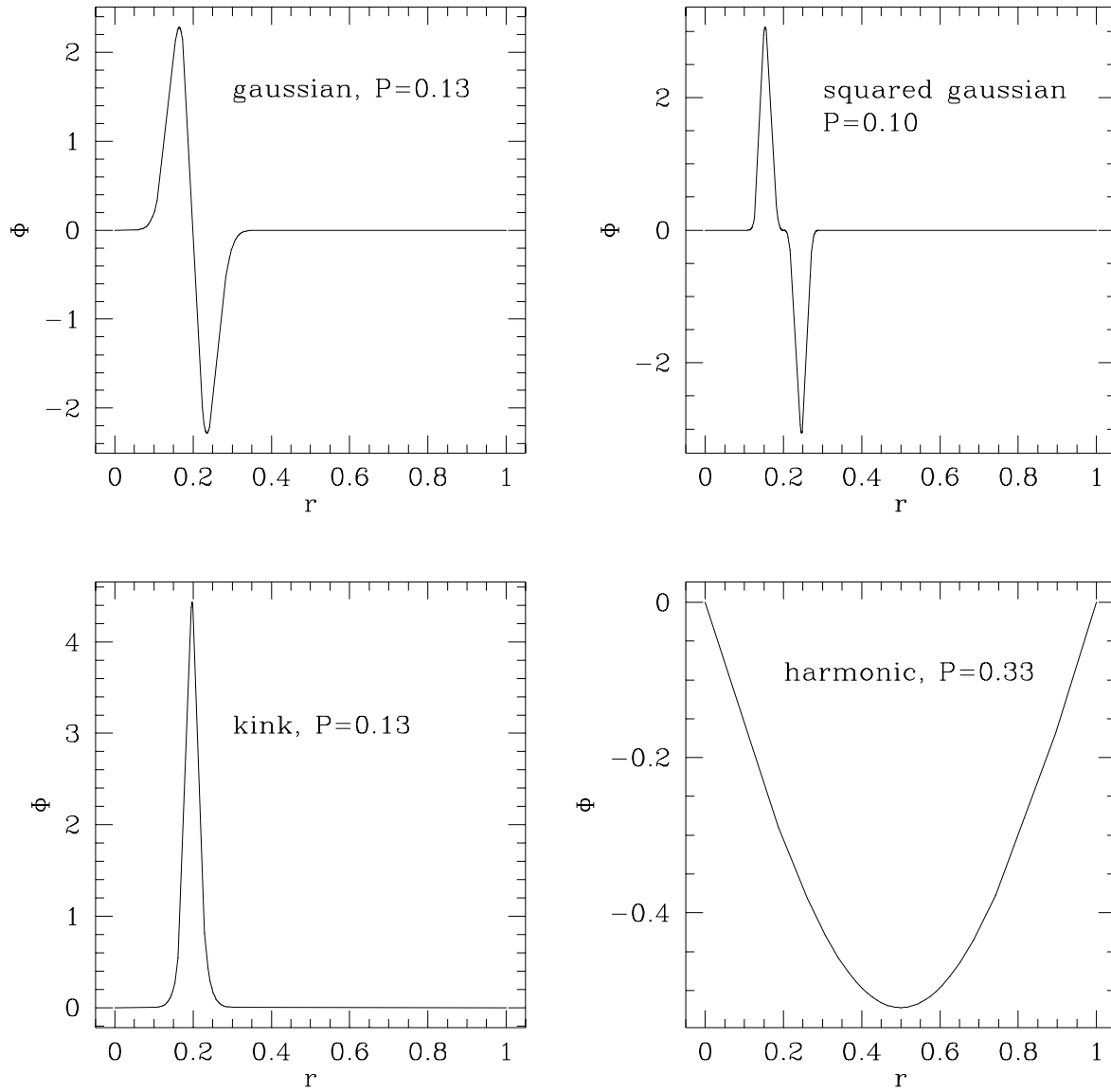


Figure 1: $\Phi(r, 0) = \phi_{,r}(r, 0)$ for each family of initial data studied. The three compact families are initially ingoing, thus $\Pi(r, 0) = \Phi(r, 0)$, while the harmonic function is time-symmetric with $\Pi(r, 0) = 0$ ($\ell = 2/\pi$, so \mathcal{I} is at $r = 1$).

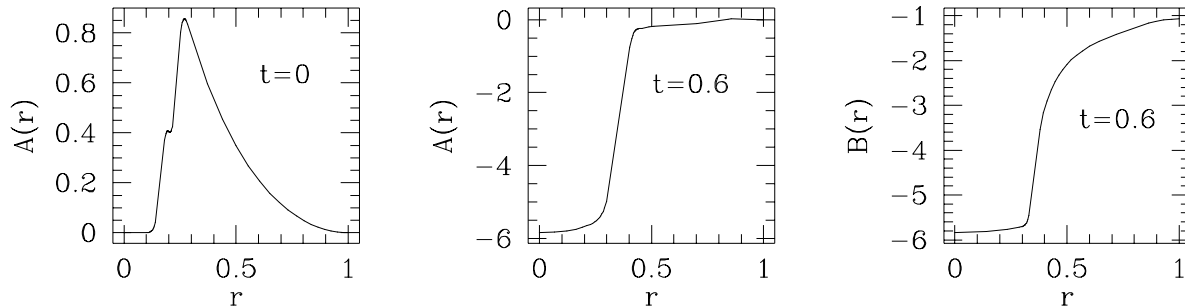


Figure 2: $A(r, 0)$ (left-most figure) for a gaussian with $P = 0.133051$, as obtained by solving the Hamiltonian constraint with $B(r, 0) = 0$. This amplitude is used as an example in section 3.3 when we discuss the singularity structure, so for reference we also show $A(r, 0.6)$ and $B(r, 0.6)$. Notice in particular how large and negative B is towards the origin, indicating that in this region of the grid we are looking at very small scales in the problem (the proper circumference element is $\bar{r} = \ell \tan(r/\ell)e^B$).

coincides with the place where the initial mass estimate dips to near zero (though for the harmonic data—as mentioned in the caption of Fig. 5—for amplitudes a little larger than P^* an apparent horizon first forms further out, engulfing the one that is about to form at the smaller radius; see also Fig. 7).

Near this threshold, it turns out that shortly after the initial implosion, the scalar field and geometry close to the origin evolve towards a universal, continuously self-similar (CSS) form. We remind the reader that a function which is CSS depends only on a single scale-invariant variable x . Now, the coordinates (r, t) in which we solve the equations of motion are *not* well-adapted to self-similarity. However, after some experimentation we found that a natural scale-invariant independent variable in our system is

$$x = \frac{\bar{r}}{t_c}, \quad (41)$$

where $\bar{r} = \ell \tan(r/\ell)e^B$ is proportional to the proper circumference of an $r = \text{constant}$ ring, and t_c is proper time as measured by the central ($r = 0$) observer. By convention, t_c is negative and increases to the accumulation point $t_c^* \equiv 0$. To better visualize the CSS behavior, we also transform to logarithmic coordinates:

$$Z \equiv \ln(\bar{r}), \quad T \equiv -\ln(t_c). \quad (42)$$

A CSS function, $f(x) = f(e^{Z+T})$, then looks like a wave propagating to the left with unit velocity as T increases to ∞ .

Figs. 9–12 show scale-invariant functions $\phi_{,Z}(Z, T)$, $\phi_{,ZZ}(Z, T)$ (the second derivative better demonstrates the “wave nature” of the critical solution), the mass aspect $M(Z, T)$, and $(\bar{r}^2 R)(Z, T)$, for a gaussian evolution with $P = 0.133059219$, which is ‘close’ to the critical solution ($\ln(P - P^*) = -17.5$; see sec. 3.2.1). In principle, the closer to criticality we tune the initial pulse, the longer the scale-invariant behavior should persist in logarithmic space. In practice, of course, finite computational precision and grid resolution prohibits fine-tuning to arbitrary accuracy—the figures plotted here show data which is about as close to criticality as we can get with 8192 grid points. In terms of the mass aspect in Fig. 11, one can surmise that the critical solution is (locally) a kink-like transition from the AdS value $M = -1$ to a zero mass state; though, interestingly enough, the value of the curvature scalar R at the origin diverges like $1/t_c^2$ as one approaches the accumulation point (we will discuss this in more detail below; also, bear in mind that in Fig. 12 we are plotting $\bar{r}^2 R$, not R itself). This behavior of the mass aspect *suggests* that the transition at

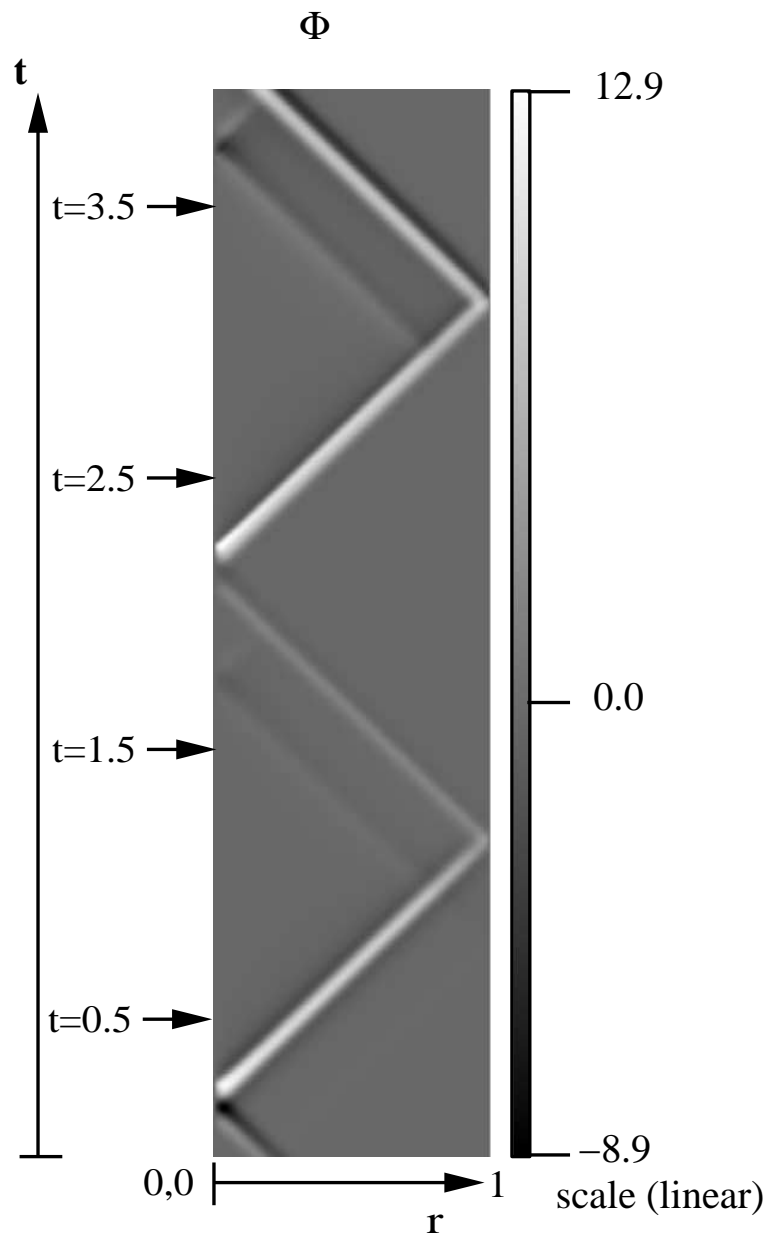


Figure 3: A plot of $\Phi(r, t)$, the spatial gradient of the scalar field, for sample gaussian initial data with $P = 0.1302$. In this case, a black hole is *not* formed. This plot clearly demonstrates the nature of the Dirichlet boundary conditions on ϕ at $\mathcal{I} (r = 1$ in these coordinates). Even though a black hole does not form, back reaction *is* significant here—notice the non-linear interaction between ingoing and outgoing components of the field: when the ingoing and outgoing pulses cross, the ingoing component is amplified, while at the same time the outgoing component is suppressed. The effect is most apparent on this plot at around $t = 3$ near the outer boundary; and note that the initial outgoing component of the field is quite small and not visible in the picture.

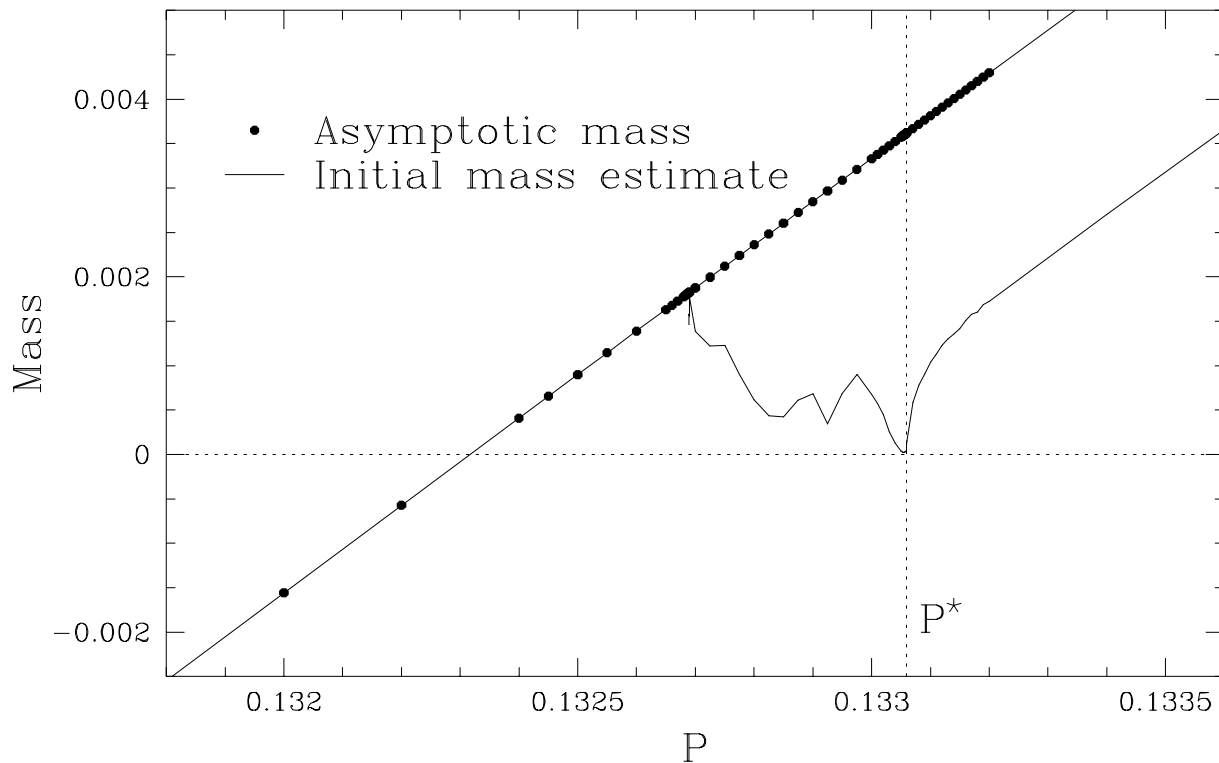


Figure 4: Asymptotic mass as a function of pulse amplitude for an initially ingoing gaussian (27) of width 0.05, centered at $r = 0.2$ in a cosmology with $\ell = 2/\pi$. For the amplitudes that formed an apparent horizon within the simulation time of $t = 2$, the mass estimate at time of AH formation is also shown (it is not clear in the figure but this curve does not touch the asymptotic mass curve). The dashed vertical line, labeled by P^* , is the critical amplitude—see sec. 3.2.

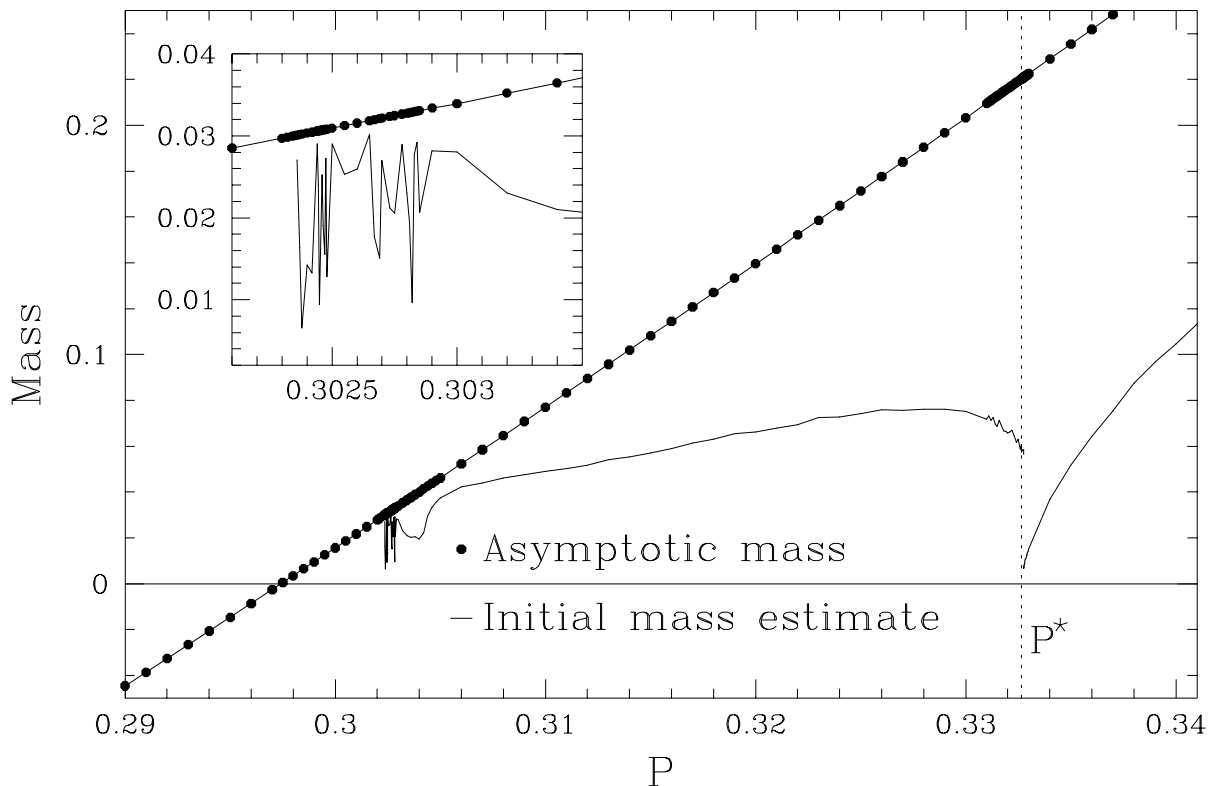


Figure 5: Asymptotic mass as a function of pulse amplitude for the time-symmetric $n = 1$ harmonic function (29). For the amplitudes that formed an apparent horizon within the simulation time of $t = 50$, the mass estimate at time of AH formation is also shown. The dashed vertical line, labeled by P^* , is the critical amplitude as discussed in sec. 3.2. Notice the discontinuity of the initial mass estimate curve just to the right of P^* , and compare the gaussian case in Fig. 4. The reason for the sudden jump, and difference from the gaussian case, is that around $t = 1$ for those amplitudes near P^* an apparent horizon is close to forming in two locations; to the left of the discontinuity it first forms at larger radii, to the right at smaller (see Fig. 7).

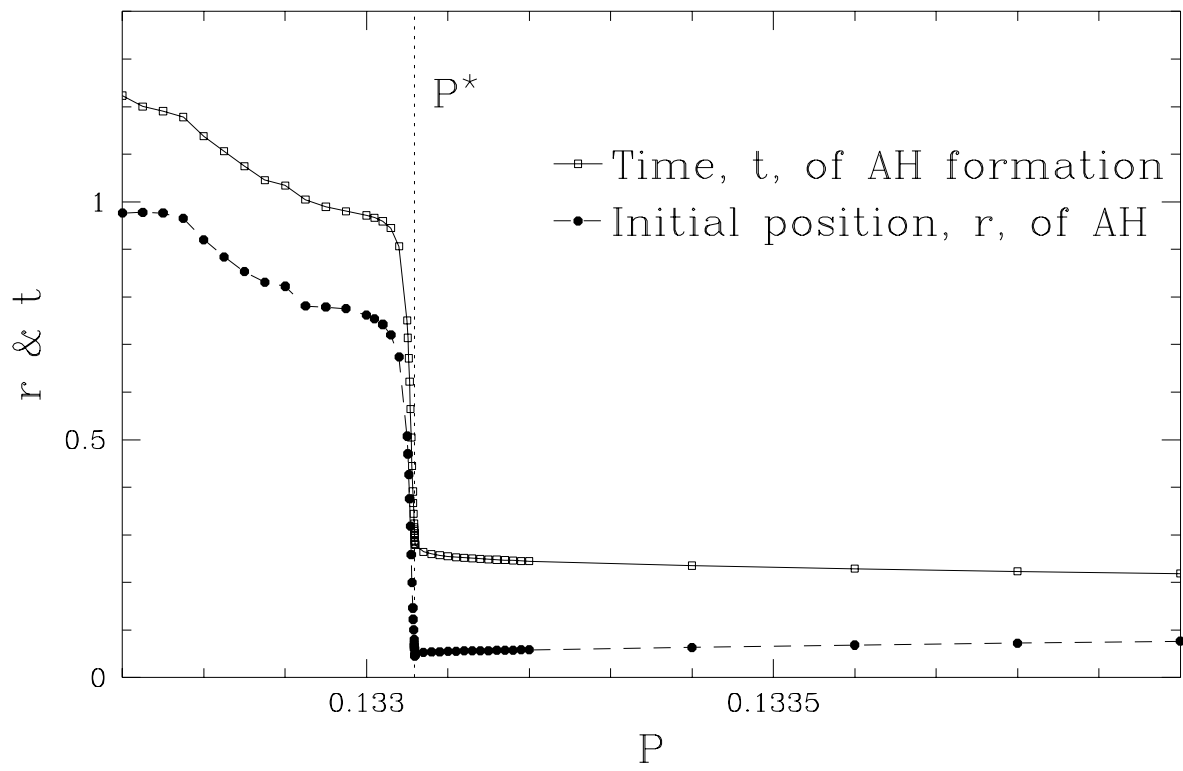


Figure 6: The initial coordinate position (r) and time (t) of AH formation for the same set of amplitudes as in Fig. 4 for the gaussian family (if an AH formed within $t = 2$).

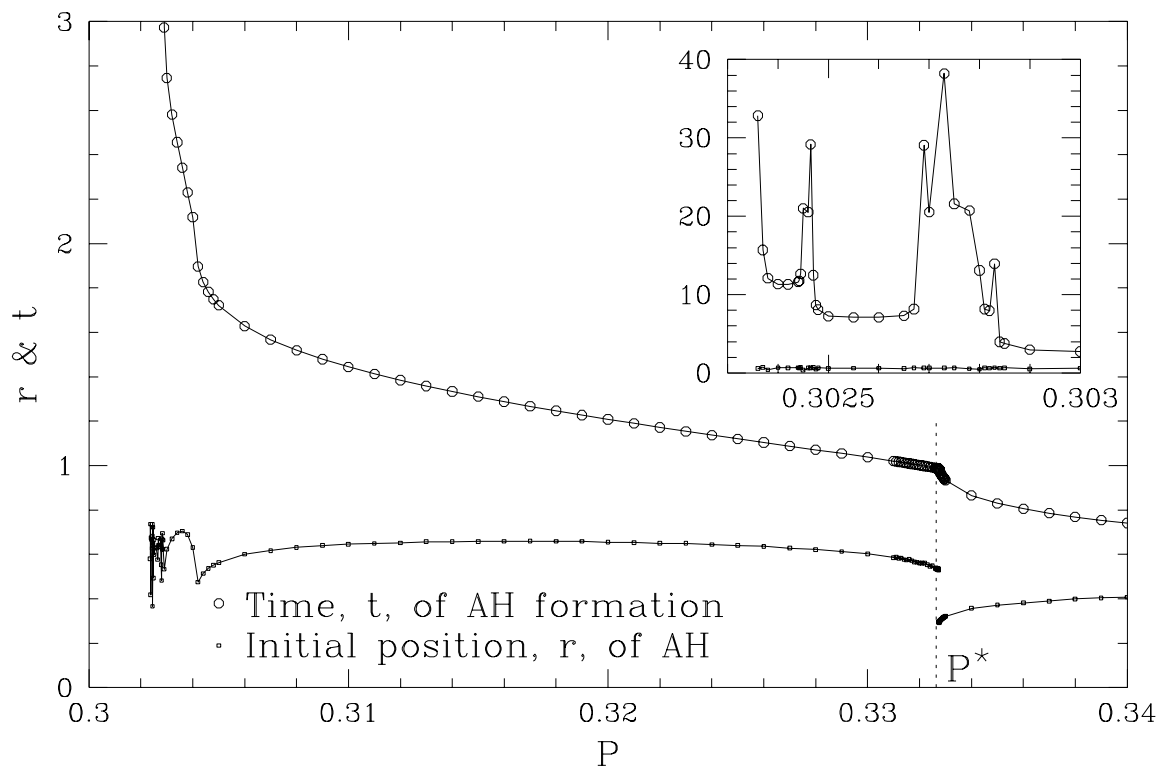


Figure 7: The initial coordinate position (r) and time (t) of AH formation for the same set of amplitudes as in Fig. 5 for the harmonic family (if an AH formed within $t = 50$).

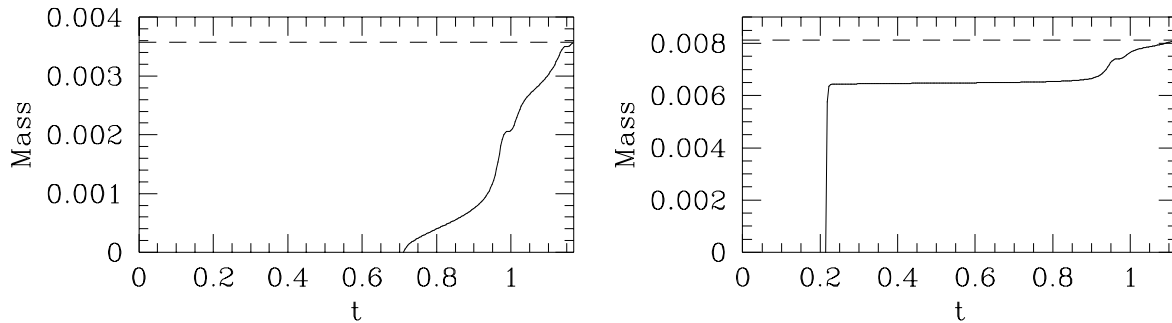


Figure 8: Black hole mass estimates as a function of time for gaussians with $P = 0.133051$ (left) and $P = 0.1340$ (right). The horizontal dashed lines denote the asymptotic masses of the spacetimes. For the less massive pulse on the left, the apparent horizon forms after the initial implosion when the field is mostly outgoing, and the energy gradually accretes onto the black hole. The more massive pulse on the right forms a black hole on the initial implosion, capturing almost all of the scalar field energy except for a small piece that initially traveled outwards from $t = 0$. This piece eventually bounces off \mathcal{I} then falls into the black hole. Note that the smaller amplitude is less than the critical value, P^* , as defined in sec. 3.2, while the larger amplitude is super-critical.

the critical point is Type II—in other words, there is no lower, positive bound on the mass of black holes that can be formed by the scalar field.

Fig. 13 demonstrates the universality of the solution in the critical regime. Here we plot $\phi_{,ZZ}$ (as in Fig. 10 for the gaussian) at the same time T for each family in a near-critical evolution. The harmonic function appears to have a slightly larger amplitude, but, as we shall now argue, this is apparently just a slicing effect. As mentioned in sec. 2.2, because of the gauge that we use, and since we choose to solve for $A(r, 0)$ and $A_{,t}(r, 0)$ using the constraint equations (8) and (9), the only slicing freedom we have remaining is in the initial conditions for $B(r, 0)$ and $B_{,t}(r, 0)$. Once $B(r, 0)$ and $B_{,t}(r, 0)$ are specified, we have no control over the manner in which the slice evolves. For the three compact, ingoing families, the critical behavior develops at times ranging from $t = 0.25$ to $t = 0.30$, and because of the similar initial spatial distribution of the energy densities, the evolution has proceeded along very similar slices. On the other hand, the harmonic data approaches the critical solution at about $t = 1.25$, at which point the slice has evolved quite differently from the other three families near their respective critical times (we note, however, that by plotting as a function of T we *do* “match” the slices at the origin). To demonstrate that the slices evolve differently, we plot in Fig. 14 the normalized inner product between $\partial/\partial t_c$ (in an \bar{r}, t_c coordinate basis) and ∇t_c for the 4 families, at the same time used in Fig. 13. This inner product is the Lorentz gamma factor, W (assuming the vectors are time-like), between $\bar{r} = \text{constant}$ observers, and those moving normal to the hypersurface $t_c = \text{constant}$:

$$W = \frac{|(\partial/\partial t_c)^\alpha \nabla_\alpha t_c|}{|\partial/\partial t_c| |\nabla t_c|}. \quad (43)$$

This quantity will be the same along identical slices of a spacetime (since such slices will have the same normal vectors); thus the harmonic solution slice is clearly different as one moves away from the origin. Another interesting feature of this plot for the harmonic data is that it shows gravitational collapse occurring a short distance away from the unfolding critical behavior, since, to the right of the peak, the vector $\partial/\partial t_c$ has become space-like (equivalently the surface $\bar{r} = \text{constant}$ has become space-like—see the discussion on the singularity structure in sec. 3.3, and in particular Fig. 20). At this point in parameter space for the harmonic function there is a lot more mass in the spacetime than that involved in the critical evolution, and this is causing an apparent horizon to form at a larger radius (see Figs. 5 and 7). Presumably, for smaller

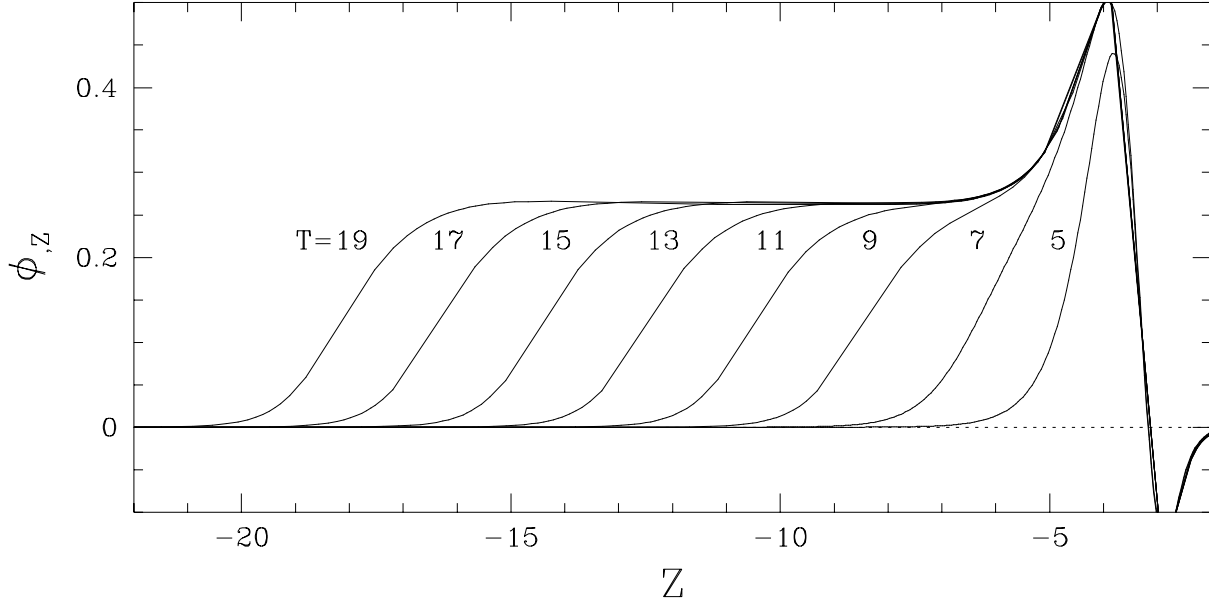


Figure 9: $\phi_{,Z}(Z, T)$ (see (42) for the definition of Z and T coordinates), for gaussian initial (27) data with $P = 0.133059219$, $\sigma = 0.05$, $n = 1$ and $r_0 = 0.2$ in an $\ell = 2/\pi$ cosmology. This function of ϕ is scale-invariant in the critical regime, which unfolds roughly between $T \approx 8$ and $T \approx 19$ (though, interestingly, the scale-invariance seems to persist for longer in the scalar field than the geometric quantities—see Figs. 11 and 12).

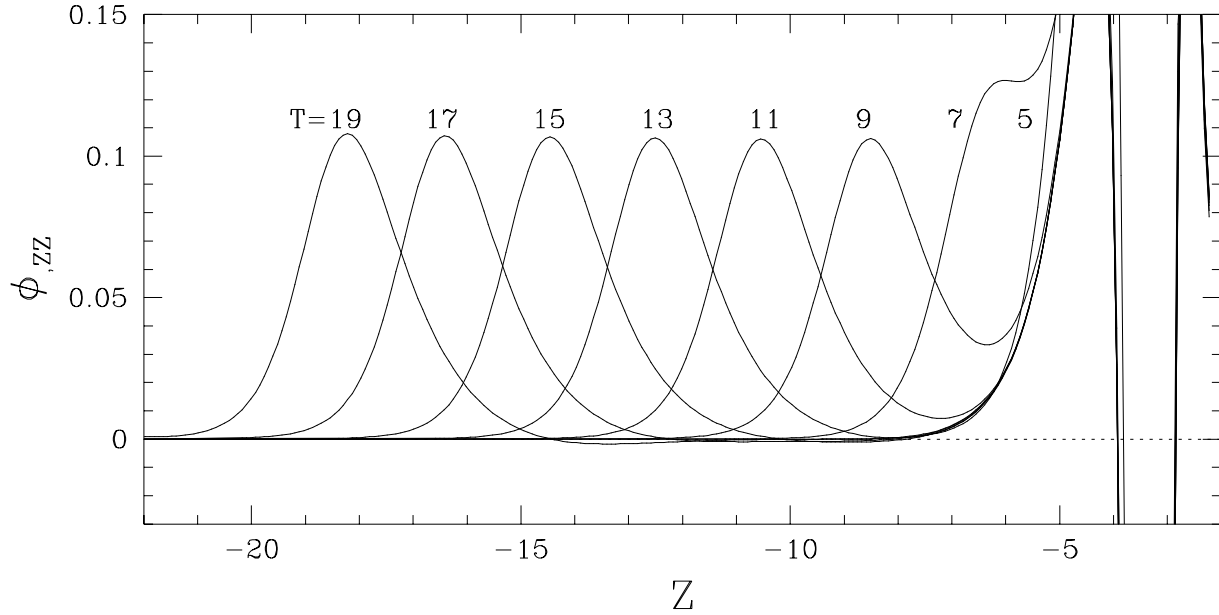


Figure 10: $\phi_{,ZZ}(Z, T)$, i.e. the derivative of the function plotted in Fig. 9.

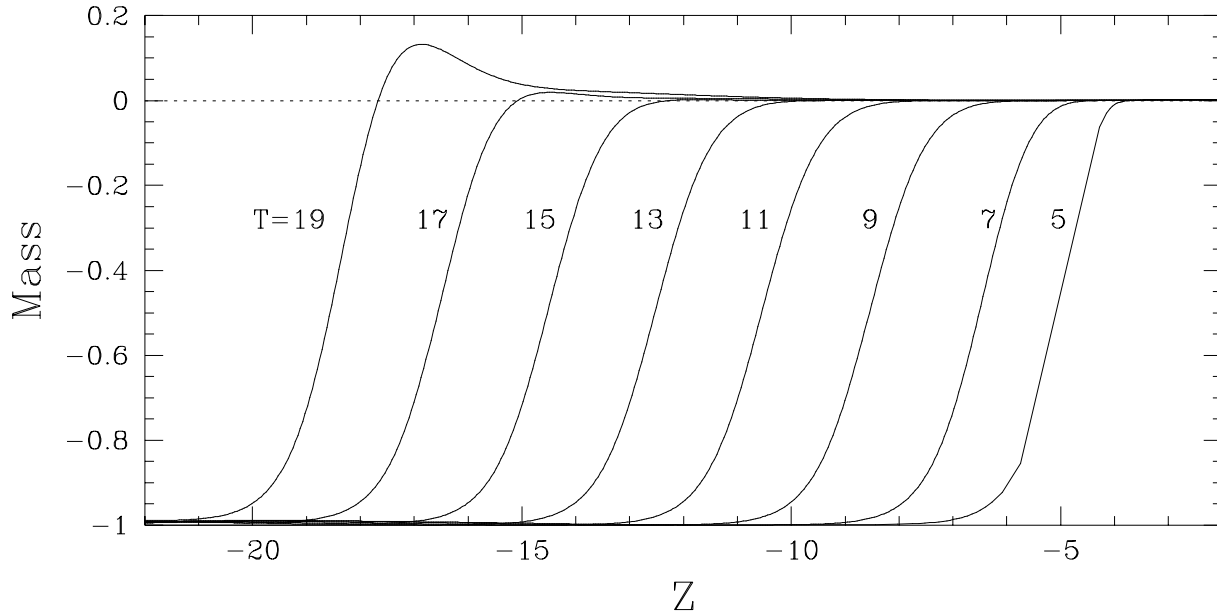


Figure 11: The mass aspect, $M(Z, T)$, for the same solution shown in Fig. 9. That M becomes slightly non-monotonic at late times is probably due to numerical error—this is a super-critical evolution, and the metric variables are already growing rapidly around $T = 19$.

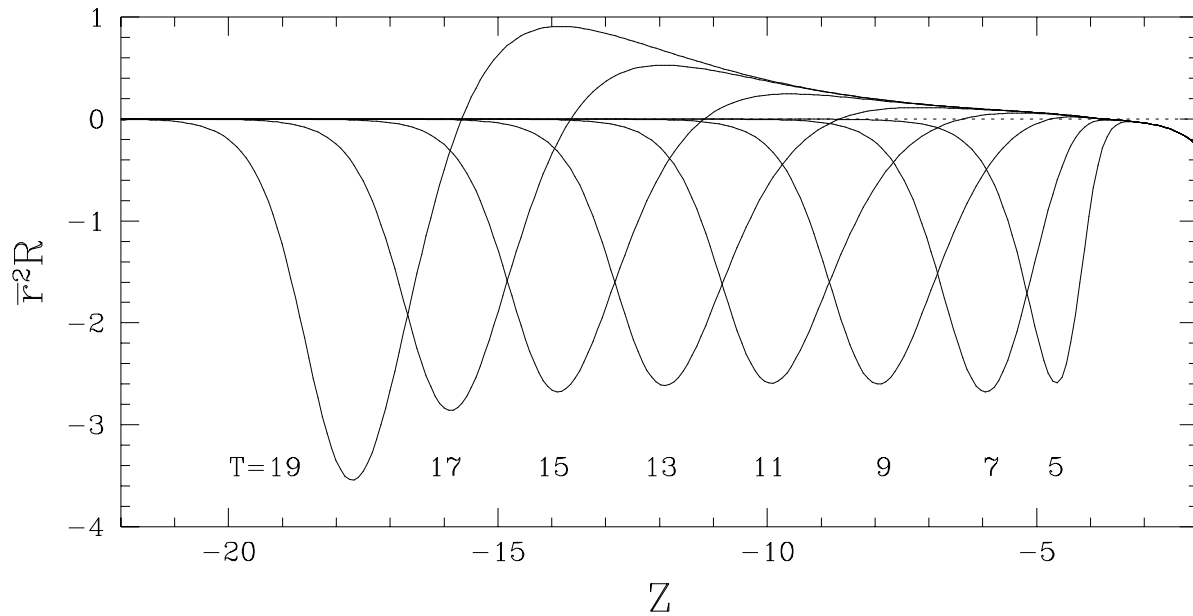


Figure 12: The Ricci scalar multiplied by \bar{r}^2 (a scale-invariant combination in the critical regime) for the same solution shown in Fig. 9.

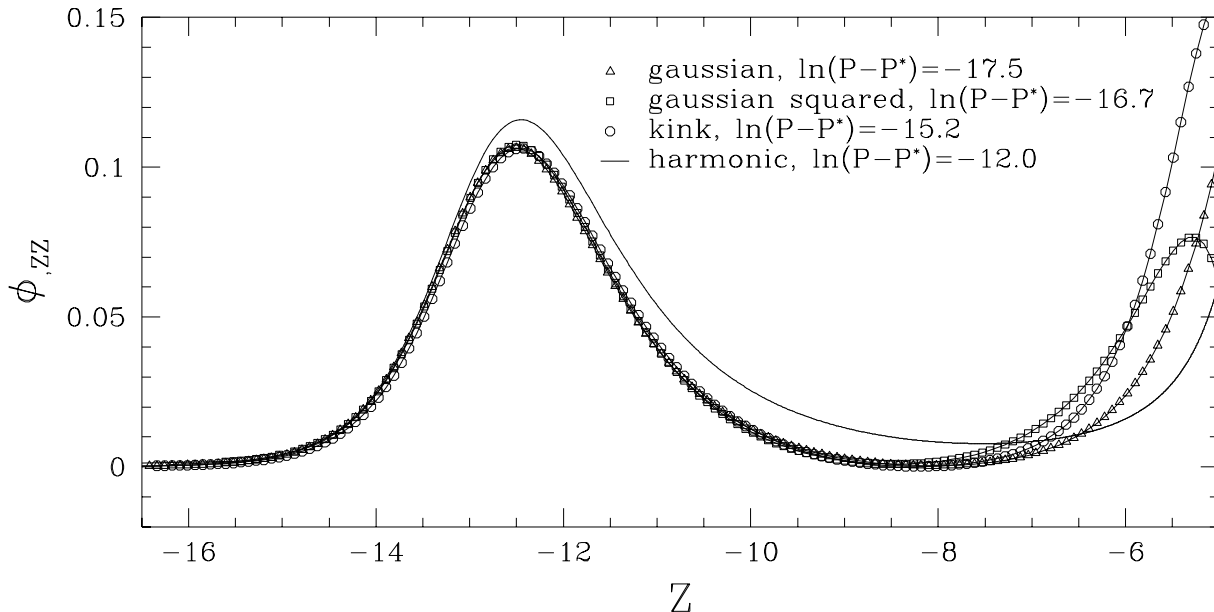


Figure 13: A composite of the scale-invariant function $\phi_{,ZZ}(Z, T)$ for the near critical solutions of the four families of initial data considered, demonstrating universality of the solution in the critical limit. The data is plotted at $T = 13$ (compare Fig. 10). The harmonic profile appears somewhat different than the others due to a slicing effect, as explained in the text (also see Figs. 14 and 15). See Fig. 16 for the values of P^* for each family.

amplitudes one could tune to a threshold solution after several light-crossing times, and perhaps then one would more cleanly uncover the critical solution.

To give more evidence that all the solutions are indeed approaching a universal one in the critical regime, we need to compare them on a common spacetime slice. In Fig. 15 we show the same function of the scalar field as in Fig. 13 transformed to a Christodoulou type coordinate system (\bar{r}, v) , where a $v = \text{constant}$ curve is an ingoing null geodesic [20]. We normalized v so that $dv = dt_c$ at the origin; i.e. v also measures central proper time. Thus comparing solutions on the same $v = \text{constant}$ surface removes any slicing ambiguity⁶. As can be seen from the figure, the transformed solutions are all quite similar, though we lose some accuracy in the transformation (which is why we have elected not to use these coordinates in all of the plots in Figs. 9 - 13).

3.2.1 The scaling exponent γ

Another characteristic feature of Type II critical behavior in gravitational collapse is the universal scaling exponent γ in the relation $M = K(p - p^*)^{2\gamma}$. To measure this relationship in the current context, one needs to wait for the system to settle down to a steady-state to ensure that the apparent horizon is coincident with the event horizon, and hence that the mass estimate (38) gives the correct mass. In AdS, the boundary conditions at \mathcal{I} prevent us from performing this measurement—initially outgoing radiation that did not contribute to the near-critical black hole formation will eventually reflect off \mathcal{I} and pollute our measurement. However, as discussed by Garfinkle and Duncan [12], in the near-critical regime (above or below p^*) any quantity with dimension L^q , where L is a length scale, should exhibit a scaling relation with an exponent of $q\gamma$. Thus, following those authors, we find the maximum value attained by the Ricci scalar R at $r = 0$ in sub-critical evolution for $t_c < 0$. Plots of $\max_{t < t_c} \ln |R(0, t)|$ vs. $\ln(P^* - P)$ for the four families studied

⁶we are grateful to David Garfinkle for suggesting this procedure to us

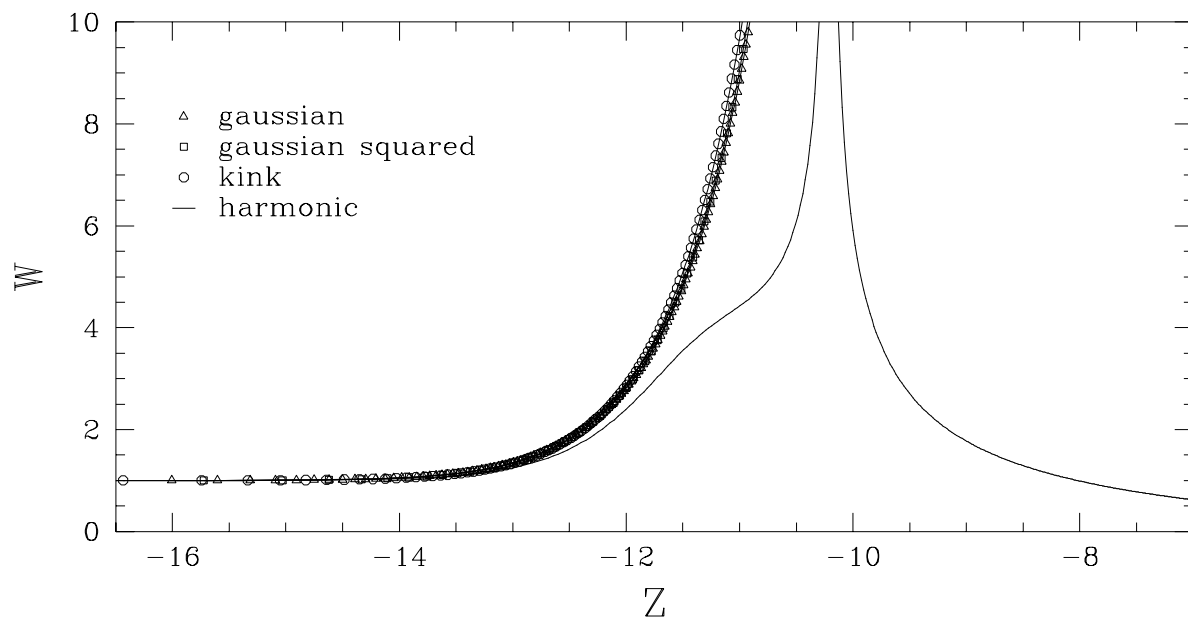


Figure 14: The Lorentz gamma factor W (43) between $\bar{r} = \text{constant}$ observer world-lines and those travelling normal to the hypersurface $t_c = \text{constant}$, at $T = 13$ for the 4 near-critical solutions as in Fig. 13. The difference between the three initially ingoing families and the harmonic one indicates that we are looking at differing slices of spacetime as we move away from $r = 0$. In fact, the discontinuous peak in γ for the harmonic solution at around $Z = -10.2$ shows that the $\bar{r} = \text{constant}$ surface has become space-like to the right of this point, indicating a region undergoing gravitational collapse.

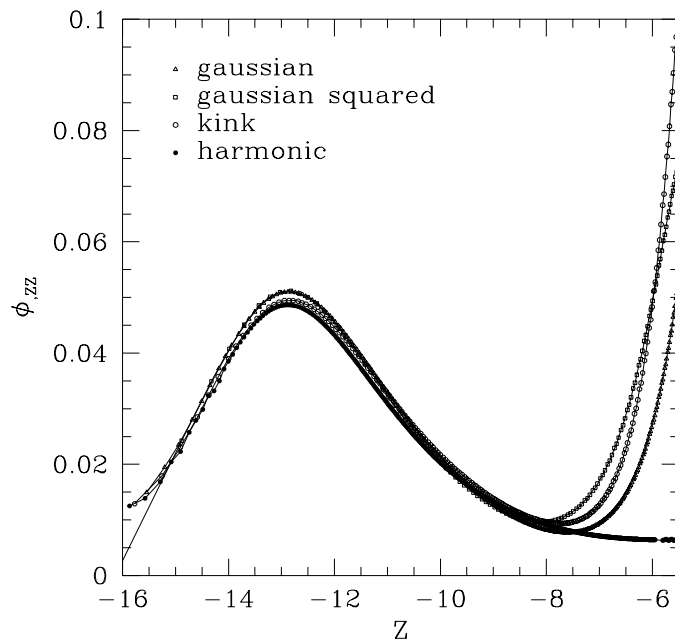


Figure 15: The function $\phi_{,ZZ}(Z, v)$ for the same solutions shown in Fig. 13. $v = \text{constant}$ is an ingoing null geodesic, chosen here to intersect the origin at $T = -\ln t_c = 13$ in all cases, and along this hypersurface we plot as a function of $Z = \ln \bar{r}$. This coordinate system completely fixes the spacetime slice along which we are comparing solutions (at the expense of some loss of accuracy during the transformation), and gives additional evidence that there *is* a universal critical solution.

is shown in Fig. 16. Since $R \propto L^{-2}$, these figures show that the scaling exponent γ of the 2+1D AdS Klein-Gordon system is about 1.2 ± 0.05 .

Notice that the mass aspect M as defined in (33) is dimensionless (which is consistent with the scale-invariance of M as plotted in Fig. 11). On the other hand, when we keep ℓ fixed and vary P , the resulting black hole mass (being proportional to r_{ah}^2) has a length scale of 2, so one would expect the mass-parameter scaling relationship for BTZ black holes to go like $M = K(P - P^*)^{2\gamma}$, where γ is the same value $1.15 - 1.25$ found above for the scaling of R . The initial-mass estimate curves as shown in Figs. 4 and 5 *do* roughly exhibit this scaling behavior for $P > P^*$.

3.2.2 Critical behavior in the presence of a point particle

Here we briefly show how the presence of a point particle (angle deficit) alters the critical solution. The particle contributes to the mass of the spacetime (36), so the more massive the particle (up to the maximum $M_{PP} = 1$ in our units) the less scalar field energy is needed to form a black hole, and consequently we have smaller amplitudes, P^* , at threshold. Interestingly, we find the *same* critical solution in all cases (see Fig. 17 for 3 examples), the only noticeable differences being a systematic phase shift in T related to the mass of the particle. The kink-like transition in the mass aspect has the same shape as well, but it ranges from the particle mass at $r = 0$ to $M = 0$. To within the resolution of our simulations (which was at 2048 grid-points in this case) the critical exponent is also the same, namely within the range $\gamma = 1.15$ to 1.25 .

3.2.3 The critical solution from a CSS ansatz?

Given that we have self-similar behavior in the critical regime, it would be useful to find the exact solution assuming a CSS ansatz. Traditionally this is done by assuming the existence of a homothetic Killing vector. ξ (see [6])

$$\mathcal{L}_\xi g_{ab} = 2g_{ab}. \quad (44)$$

This implies that in coordinates adapted to the homotheticity, so that $\xi = \partial/\partial\tau$, each component of g_{ab} has the form $e^{2\tau}f$, for some function f independent of τ . Furthermore, $\mathcal{L}_\xi R_{ab} = 0$, so that R_{ab} and hence the Einstein tensor G_{ab} are independent of τ . This ansatz is not consistent with the field equations (1) in the presence of the cosmological constant if we assume that the scalar field is self-similar (see [25]), as we observe in the collapse simulations. Essentially, the scalar field stress-energy tensor (2) would need to decouple into a piece that exactly cancels the cosmological constant term plus a scale-invariant term, but we do not think that this is possible for a minimally-coupled scalar field.

It may be that in the 2+1D AdS system a different symmetry, such as a conformal Killing vector, would be needed to generate the critical solution. Or perhaps the critical solution is only approximately homothetic over a limited region of the spacetime. Nevertheless, we have not yet found a symmetry-reduced system that reproduces the observed critical behavior.⁷

3.3 Singularity structure

In all of the solutions that we have studied so far we find that after an apparent horizon forms what appears to be a spacelike curvature singularity develops within the horizon. Specifically, the surface of excision along which the metric variables A and B and, consequently, the curvature invariants begin to diverge, is spacelike. By itself, demonstrating a spacelike surface of arbitrarily large curvature is not sufficient to prove that the singularity is spacelike—a counter-example would be the mass-inflation null singularity [22]⁸. However, if we extrapolate to the surface of infinite curvature, based upon the growth of the Ricci scalar prior to excision, we still find a spacelike surface (in fact, R grows so rapidly prior to excision—roughly like $1/t^4$ along an $r = \text{constant}$ surface if we translate t to zero at the singularity—that the surface of infinite curvature essentially coincides with the excision surface at the resolution of Fig 19 below). In addition,

⁷Note added in preparation: David Garfinkle has very recently found a CSS solution in the limit where the cosmological constant vanishes that appears to quite accurately describe the critical solution that we have found [21]. His result is quite intriguing—the cosmological constant is *essential* for black holes to form, yet apparently it plays very little role in the solution at the *threshold* of formation!

⁸We are grateful to Lior Burko for pointing this out to us

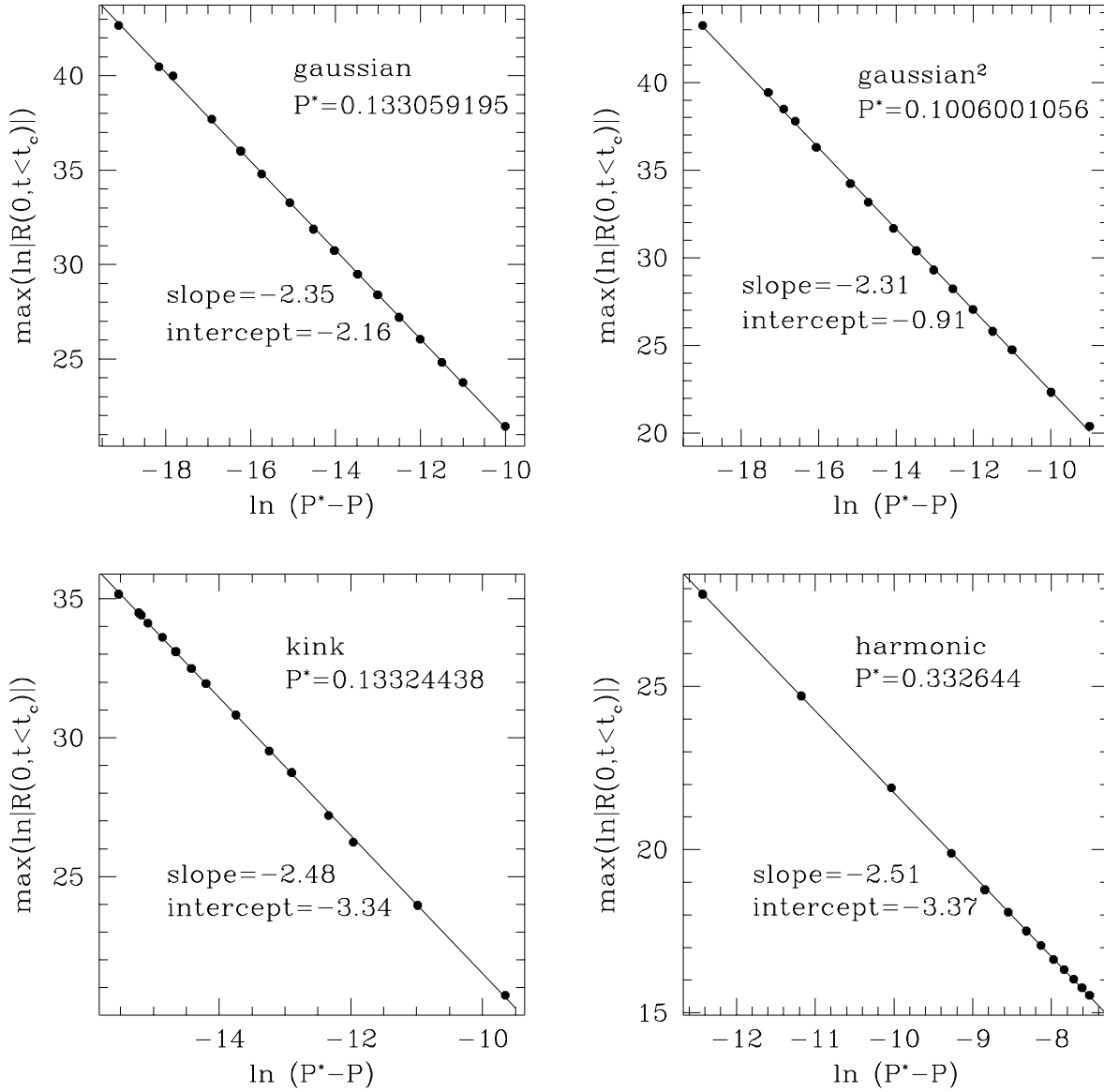


Figure 16: The maximum of $\ln|R(0, t < t_c)|$ as a function of $\ln(P^* - P)$ for sub-critical ($P < P^*$) evolutions of the 4 families of initial data considered. These plots indicate that the maximum of $R(0, t < t_c)$ attained during evolution is proportional to $(P^* - P)^{-2\gamma}$, with $\gamma \approx 1.15 - 1.25$.

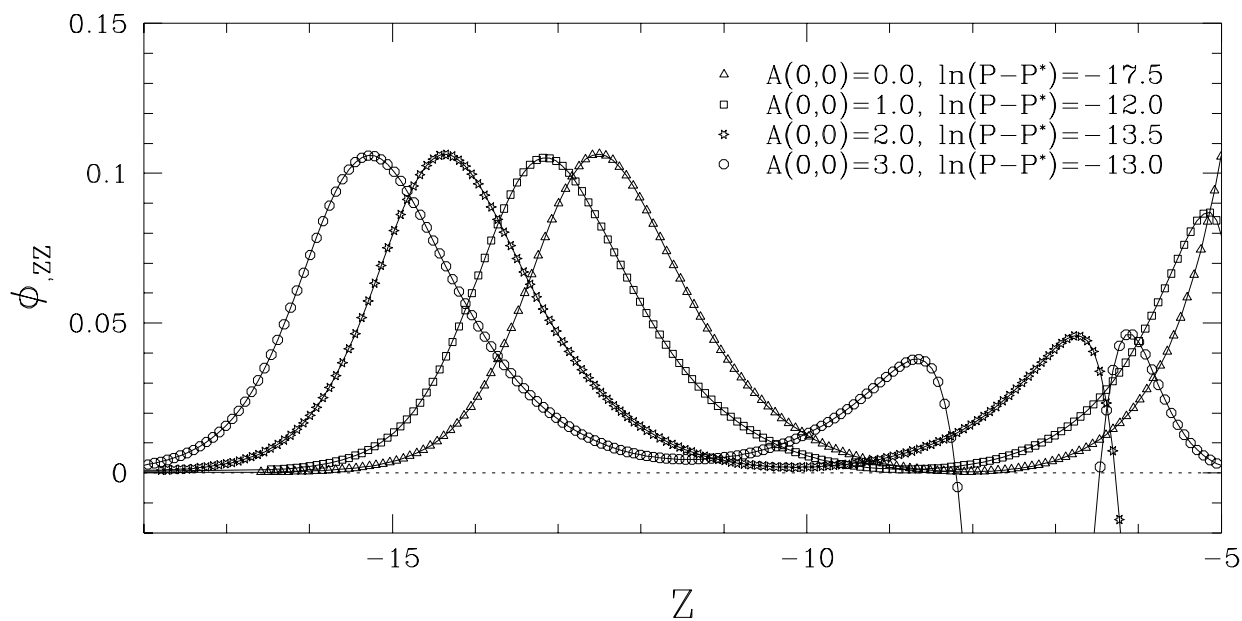


Figure 17: A composite of the scale-invariant function $\phi_{,ZZ}(Z, T)$ at $T = 13$ for the near critical solutions of the gaussian family ($\sigma = 0.05, r_0 = 0.2$) with 4 different initial values for $A(0, 0)$ —0, 1, 2 and 3, corresponding to the presence of point particles at the origin with masses 0, 0.864665, 0.981684 and 0.997521 respectively (36). It is striking that these solutions only differ by a phase in T related to the particle masses; they have evolved to the same amplitude after starting with quite different initial amplitudes (namely, $P \approx 0.13, 0.078, 0.034, 0.013$ from $A = 0$ to 3).

$B(t, r) \rightarrow -\infty$ along this surface, indicating that the proper circumference measure $\ell \tan(r/\ell) e^B$ goes to zero there (see Fig. 20 below). Thus, as with vacuum BTZ black holes, this singularity is crushing⁹: any extended object reaching the singularity is forced to zero proper circumference, regardless of any angular momentum or internal pressures that the object might have.

Figs. 18 and 19 are spacetime plots (essentially Penrose diagrams) of $\Phi(r, t)$ and the Ricci scalar $R(r, t)$, respectively, for a gaussian initial pulse with $P = 0.133051$. On the pictures we have superimposed the region of trapped surfaces and the inferred event horizon of the space time, found by tracing a null ray backwards in time from the place where the AH meets \mathcal{I} on the coordinate grid. Fig. 20 show contours of proper circumference for the same solution. The point $P = 0.133051$ in parameter space is slightly sub-critical (as we have defined criticality, see Sec. 3.2)—a black hole forms because the bit of outgoing energy present at $t = 0$ bounces off \mathcal{I} and falls back onto the nearly collapsed scalar field, pushing it over the limit. This gives us a very clear view of the interior structure; for a more massive pulse the singularity forms shortly after the initial implosion, resulting in a thin sliver of an interior in (r, t) coordinates.

From Fig. 19 one can see a striking peak that forms in R after the scalar field has bounced through the origin and is travelling outwards. In this particular case R has a value of order -10^{10} in the interior, it then grows to order $+10^8$ over a very short distance before decreasing to the AdS value of $-6/\ell^2 \approx -15$. This near-discontinuous behavior in R is characteristic of sub-critical evolutions, and becomes more extreme as one nears the critical solution.

As one approaches the excised space-like surface in Fig. 19, R starts to grow very rapidly, reaching values up to $|10^{28}|$ before excision (this may not be clear on the figure—we chose the gray scale to highlight the near-discontinuous behavior in R). R actually oscillates between large positive and negative values along this surface, but our calculations are not sufficiently accurate to conclude that the oscillation is genuine. In particular, R is extremely sensitive to the difference $\Pi^2 - \Phi^2$ (see (11)), and Π^2 is usually around the same order of magnitude as Φ^2 there. We also note that the maximum value attained by R along the excised surface becomes smaller towards \mathcal{I} . This is to be expected, since in the 2+1D system, *some* scalar field is necessary to produce a value of R differing from the AdS value (again, see (11)), and as we move towards \mathcal{I} along the excised surface there is progressively less scalar field energy remaining.

4 Concluding remarks

We have studied black hole formation from the collapse of a minimally-coupled massless scalar field in 2+1 dimensional AdS spacetime. Outside of the event horizon the spacetime settles down to a BTZ form; in the interior a central, spacelike curvature singularity develops. At the threshold of black hole formation we find that the scalar field and spacetime geometry evolve towards a universal, continuously self-similar form. When a point particle is present at the origin the critical solution is shifted in central proper time by an amount related to the mass of the particle.

By examining the behavior of the curvature scalar during sub-critical evolution we deduced that the universal scaling exponent γ for this system is roughly 1.2 ± 0.05 . This value is quite different from the scaling exponent $1/2$ derived by Peleg and Steif [9] for the collapse of thin rings of dust and by Birmingham and Sen [10] for particle collisions. However, those works considered different forms of matter, and the phase transition was between black hole and naked singularity formation. Thus one would not expect the same exponent. Also, the local spacetime geometry about a dust ring or point-particles is necessarily (empty) AdS, hence such systems cannot exhibit any of the features, other than mass scaling, that are characteristic of critical gravitational collapse.

Some questions remain unanswered in this work. First, what is the exact nature of the critical solution? In other words, what is the character of the symmetry (if any) responsible for the self-similar behaviour, as the system does not appear to admit a global homothetic Killing vector¹⁰. Second, will *any* distribution

⁹or *deformationally strong*, see [23]. It is straight-forward (though tedious) to see that $r = 0$ in the non-rotating BTZ black hole is a strong singularity as defined by Tipler (though it is not a curvature singularity!). We have not repeated the formal calculations in terms of Jacobi fields in our collapse simulations, but because of the central, space-like nature of the singularity back-reaction is not likely to weakening it. Note added in revision: shortly after this paper was first published, Lior Burko studied the structure of the singularity in 2+1D AdS spacetime using a ‘quasi-homogenous’ approximation, and did find the singularity to be strong and spacelike [24].

¹⁰though, as mentioned in the footnote of sec. 3.2.3, David Garfinkle has found a CSS solution that is apparently relevant to

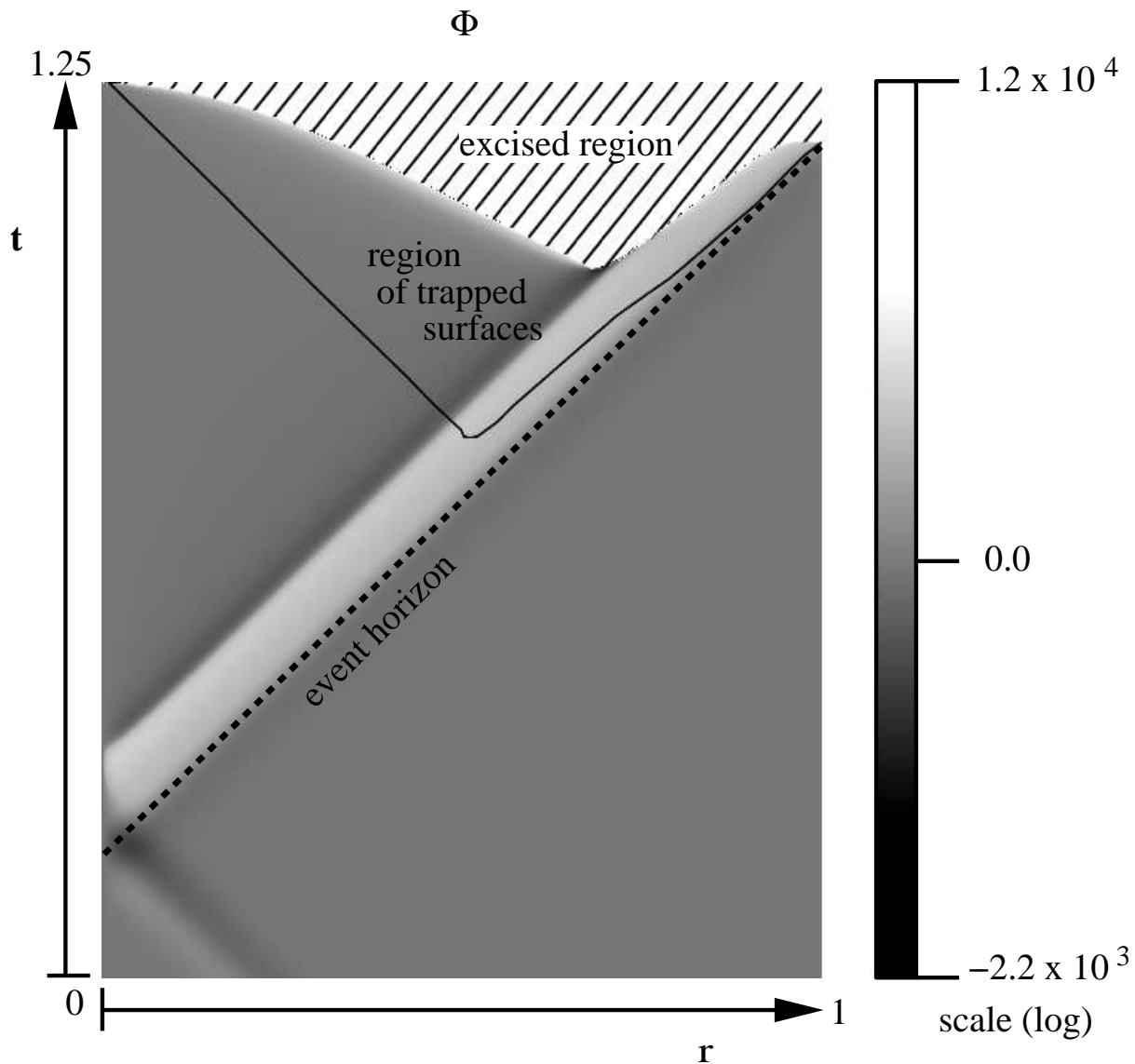


Figure 18: The gradient of the scalar field $\Phi(r, t)$ on the entire solution domain for a gaussian with $P = 0.133051$. On this picture we have also outlined the region of spacetime containing trapped surfaces, and drawn in the event horizon with a dashed line (found by tracing a null ray backwards in time from the place where the AH reaches $r = 1$ —which is also \mathcal{I} , so our coordinate system breaks down there). We stop the simulation at points where the metric variables begin to diverge (the lower boundary of the excised region), which presumably is just before a spacetime singularity forms (see Fig 19 for a similar plot of the curvature scalar).

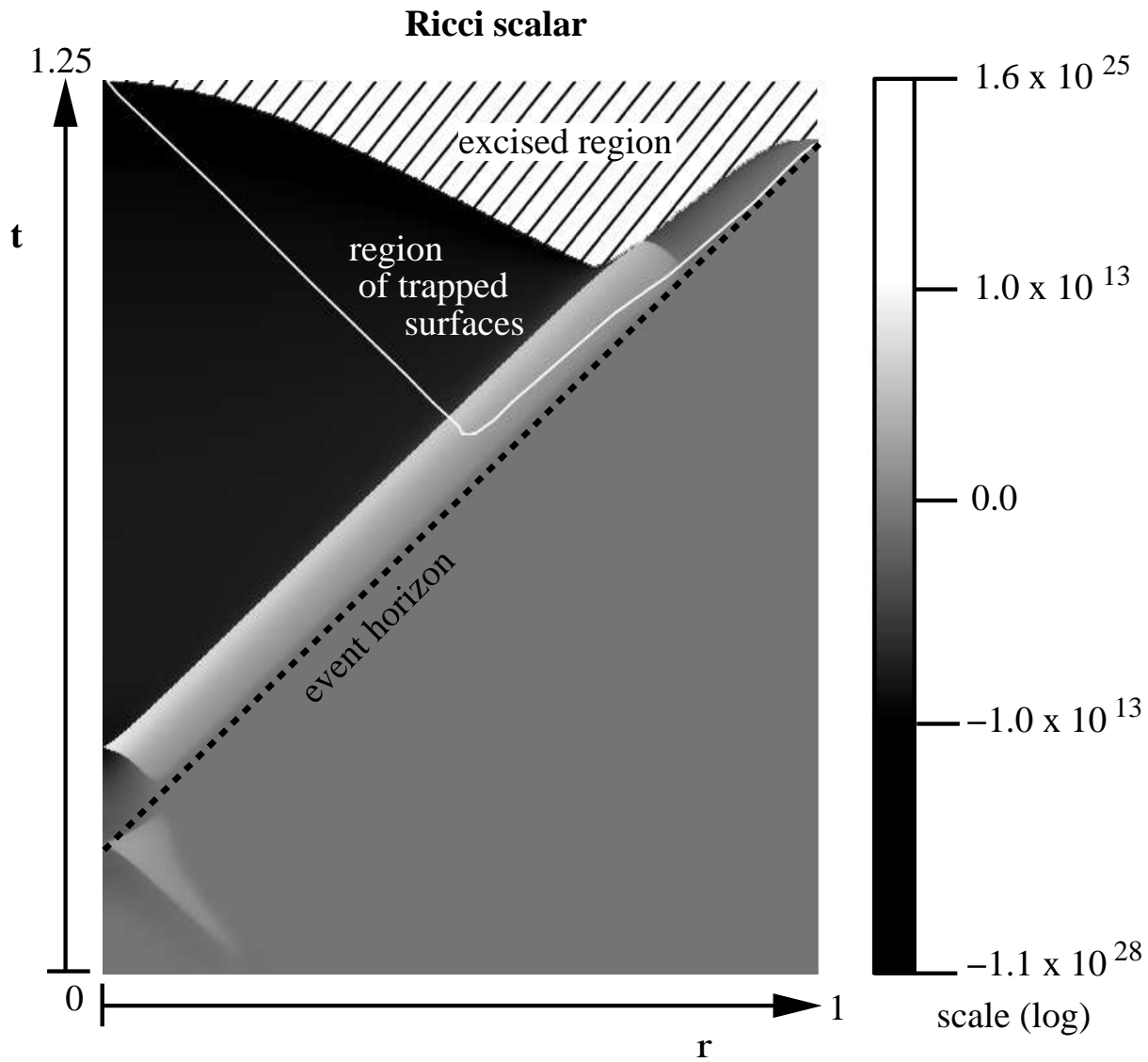


Figure 19: A plot of the Ricci scalar $R(r, t)$ for the same solution as shown in Fig. 18. During most of the evolution $|R|$ is bounded above by $\approx 10^{13}$, but shortly before reaching the excision boundary R starts to diverge rapidly, signaling the formation of a spacelike singularity.

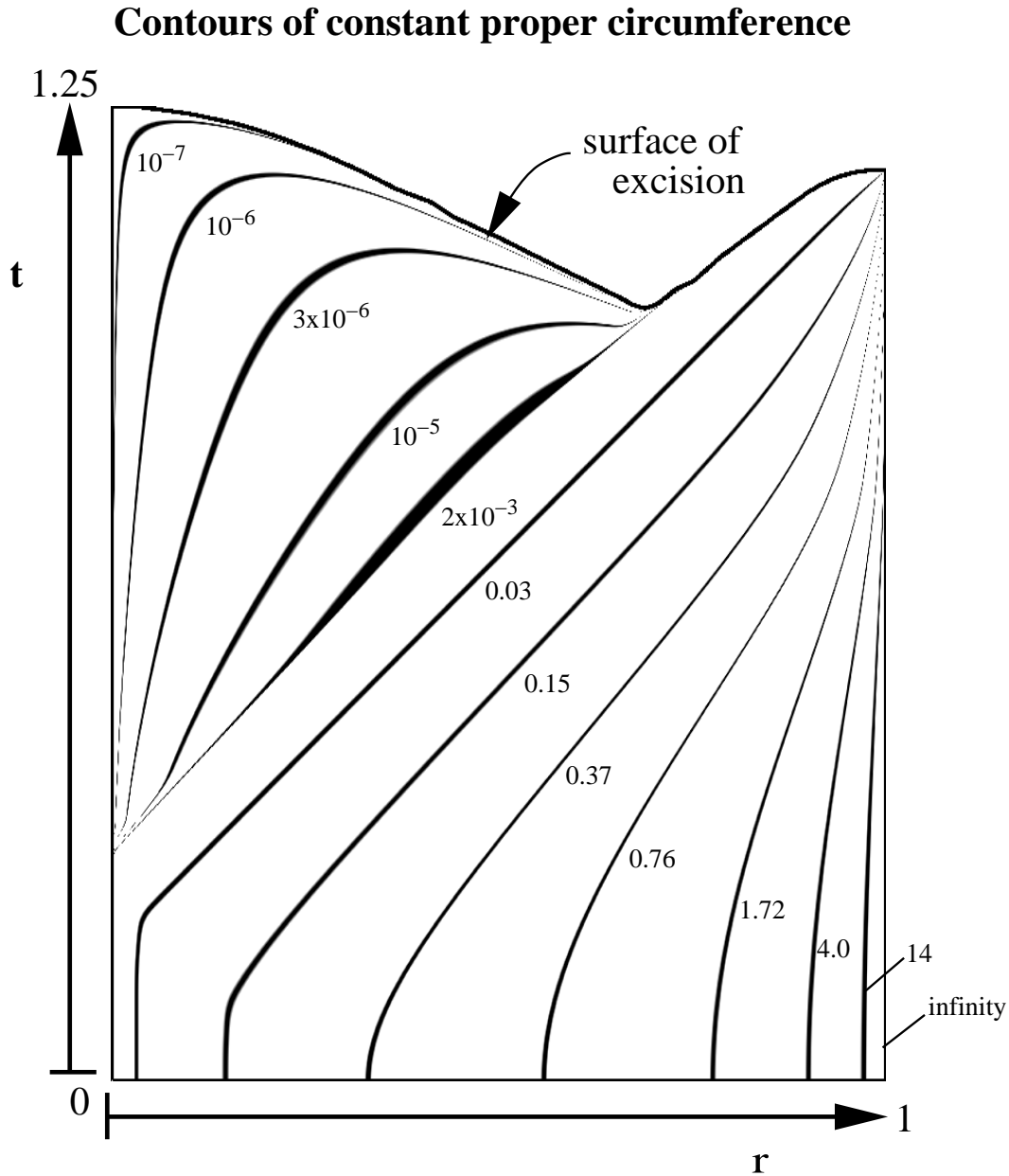


Figure 20: A contour plot of proper circumference (divided by 2π) $\bar{r} = \ell \tan(r/\ell)e^B$ for the same solution as shown in Fig. 18 (the thickness of each contour line is constant in units of proper circumference). This plot demonstrates the central nature of the singularity. Along the excised surface approaching \mathcal{I} \bar{r} also tends towards zero, though it is not clear with the limited resolution of this figure there. The event horizon asymptotes to $\bar{r} = 0.037$, i.e. just outside the $\bar{r} = 0.03$ contour.

of energy that could conceivably form a black hole (i.e. with asymptotic mass $M > 0$) eventually do so if one waits long enough (because of the Dirichlet boundary conditions imposed on the scalar field at \mathcal{I})? A third question, related to the first two, is whether the critical solution we have found is a true black-hole-formation *threshold* solution. In other words, that we have found a universal, CSS solution via a fine-tuning process indicates that this critical solution is one-mode unstable; so, does perturbing the critical solution “one way” result in a black hole, and perturbing it the “other way” cause the scalar field to remain regular, never forming a black hole? The asymptotic nature of AdS spacetime, which is ultimately responsible for the boundary conditions of the scalar field at \mathcal{I} , prevent us from answering this question in our collapse simulations.

With regards to future work, it would be useful to extend these results to different scalar-field/geometry couplings, include a mass and potential terms in the Lagrangian, and to add angular momentum to the initial data to study the formation of rotating black holes. It would also be interesting to understand the critical behavior in light of the AdS/CFT correspondence. Even though our calculation is purely classical, there should be a regime where the classical evolution is a good approximation to the full bulk theory, and consequently there should be a dual CFT description of the critical phenomena.

Acknowledgements We would like to thank David Garfinkle, Viqar Husain, Lior Burko, Iñaki Olabarrieta, Michel Olivier, Bill Unruh, Jason Ventrella, and Don Witt for many stimulating discussions. We are grateful to David Garfinkle for suggesting to us the method we used to obtain γ , as well as the use of the ingoing null coordinate system to compare near-critical solutions. MWC would particularly like to thank Robert Mann for many early discussions about this problem during the 1999 *Classical and Quantum Physics of Strong Gravitational Fields* program held at the Institute for Theoretical Physics, UC Santa Barbara. This work was supported by NSERC and by NSF PHY97-22068 and PHY94-07194. Most calculations were carried out on the vn.physics.ubc.ca Beowulf cluster which was funded by the Canadian Foundation for Innovation.

References

- [1] M. Bañados, C. Teitelboim and J. Zanelli, *Phys. Rev. Lett.* **69**, 1849 (1992)
- [2] J. M. Maldacena, *Adv. Theor. Math. Phys.* **2**, 231 (1998), hep-th/9711200.
- [3] M. Bañados, M. Henneaux, C. Teitelboim and J. Zanelli, *Phys. Rev. D.* **48**, 1506 (1993),
for generalizations to higher dimensions and multi-black holes see
D. Brill, *Phys. Rev.* **D53**, R4133 (1996),
A. Steif, *Phys. Rev.* **D53**, 5527 (1996),
S. Aminneborg, I. Bengtsson, S. Holst and P. Peldan, *Class. Quant. Grav.* **13**, 2707 (1996), gr-qc/9604005
- [4] S. Carlip, *Class. Quant. Grav.* **12**, 2853 (1995),
R.B. Mann, “Topological Black Holes—Outside Looking In”, gr-qc/9709039.
- [5] M. Choptuik, *Phys. Rev. Lett.* **70**, 9 (1993).
- [6] C. Gundlach, “Critical phenomena in gravitational collapse”, *Living Reviews* 1999-4
- [7] R. Mann and S. Ross, *Phys. Rev.* **D47**, 3319 (1993),
W.L. Smith and R.B. Mann, *Phys.Rev.* **D56**, 4942 (1997)
- [8] V. Husain, *Phys. Rev.* **D50**, 2361 (1994)
K. S. Virbhadra *Pramana* **44**, 317 (1995)
- [9] Y. Peleg and A. R. Steif, *Phys. Rev.* **D51**, 3992 (1995), gr-qc/9412023.
U. Danielsson, E. Keski-Vakkuri and M. Kruczenski, *JHEP* **0002**, 039 (2000), hep-th/9912209
U. Danielsson, E. Keski-Vakkuri and M. Kruczenski, *Nucl. Phys.* **B563**, 279 (1999)

- [10] H. Matschull, *Class. Quant. Grav.* **16**, 1069 (1999),
D. Birmingham and S. Sen, *Phys.Rev.Lett.* **84**, 1074 (2000), hep-th/9908150
- [11] V. Husain and M. Olivier, “Scalar field collapse in three-dimensional AdS spacetime”, gr-qc/0008060 (2000).
- [12] D. Garfinkle and G.C. Duncan, *Phys.Rev.* **D58**, 064024 (1998)
- [13] R.M. Wald *General Relativity*, Chicago IL, University of Chicago Press 1984
- [14] S.W. Hawking and G.F.R. Ellis, *The Large Scale Structure of Space-Time* (Cambridge: Cambridge University Press)
- [15] G.J. Galloway, K. Schleich, D.M. Witt and E. Woolgar, *Phys. Rev.* **D60**,104039 (1999)
- [16] H. Kreiss and J. Olinger, “Methods for the Approximate Solution of Time Dependent Problems”, *Global Atmospheric Research Programme, Publications Series No. 10.* (1973)
- [17] R.L. Marsa and M.W. Choptuik, “The RNPL User’s Guide”,
http://laplace.physics.ubc.ca/Members/marsa/rnpl/users_guide/users_guide.html (1995)
- [18] <http://laplace.physics.ubc.ca/People/fransp/index.html>
- [19] W.G. Unruh (1984), private communication
- [20] see D. Christodoulou, *Class. Quant. Grav.* **16**, A23 (1999), and references therein
- [21] D. Garfinkle, “An exact solution for 2+1 dimensional critical collapse”, gr-qc/0008023 (2000)
- [22] E. Poisson and W. Israel, *Phys. Rev.* **D 41**, 1796 (1990)
- [23] F.J. Tipler, *Phys. Lett. A* **64A**, 8 (1977),
A. Ori *Phys. Rev.* **D61**, 064016 (2000),
B.C. Nolan, *Phys.Rev.* **D62**, 044015 (2000), gr-qc/0001026
- [24] L.M. Burko, “Singularity in 2+1 dimensional AdS-scalar black hole”, gr-qc/0008043 (2000).
- [25] P.R. Brady, *Phys.Rev.* **D51**,4168 (1995).